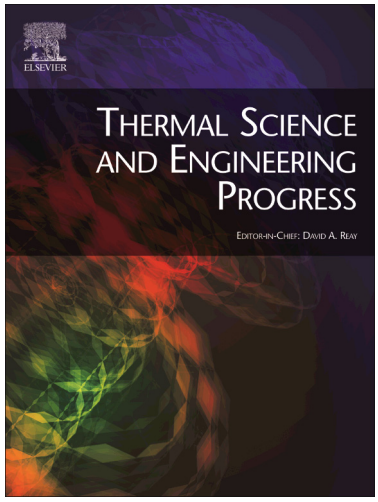

A parametric study of thermal and residual stress fields in lined pipe welding

Obeid Obeid, Giulio Alfano, Hamid Bahai, Hussam Jouhara

PII: S2451-9049(17)30291-3
DOI: https://doi.org/10.1016/j.tsep.2017.10.011
Reference: TSEP 75

To appear in: *Thermal Science and Engineering Progress*

Received Date: 12 September 2017
Revised Date: 16 October 2017
Accepted Date: 17 October 2017

Please cite this article as: O. Obeid, G. Alfano, H. Bahai, H. Jouhara, A parametric study of thermal and residual stress fields in lined pipe welding, *Thermal Science and Engineering Progress* (2017), doi: https://doi.org/10.1016/j.tsep.2017.10.011

A parametric study of thermal and residual stress fields in lined pipe welding

Obeid Obeid[1, a], Giulio Alfano[1,b], Hamid Bahai[1,c], Hussam Jouhara[1,d]

[1]College of Engineering, Design and Physical Sciences, Brunel University, UB8 3PH Uxbridge, UK

[a]obeid.obeid@brunel.ac.uk, [b]giulio.alfano@brunel.ac.uk, [c]hamid.bahai@brunel.ac.uk, [d]hussam.jouhara@brunel.ac.uk

ABSTRACT

Welded lined cylindrical structures such as boilers, pressure vessels and transportation pipes are widely used in the oil and gas industries because an inexpensive outer layer is protected from corrosion by a thinner expensive layer, which is made of a corrosion resistant alloy (CRA). Welding in the lined pipe is of two different types, where the first one, so called weld overlay (lap-weld), is deployed to seal the liner with the outer pipe whilst the other one, known as girth welding (butt-weld), is deposited to join two specimens of lined pipe together. Therefore, the precise prediction of the thermal and residual stress fields due to the combination of two different types of circumferential welding is a major concern regarding welded lined pipes to avoid sudden failure during service. Six parametric studies have been conducted primarily to examine the influence of welding properties (weld overlay and girth welding materials), geometric parameters (weld overlay and liner) and welding process parameters (heat input) on the thermal and residual stress fields. All predicted results obtained from a 3-D FE model based on the ABAQUS code are validated against small-scale experimental results. Furthermore, in this study, the effect of mesh size has been investigated.

Keywords: Lined pipe; Weld overlay; Girth welding; Thermal history; Residual stress

Nomenclature

a	Half-length of heat source (mm)
b	Depth of heat source (mm)
c	Half-width of heat source (mm)
$d\varepsilon_{ij}$	Total strain
$d\varepsilon_{ij}^{e}$	Elastic strain
$d\varepsilon_{ij}^{p}$	Plastic strain
$d\varepsilon_{ij}^{th}$	Thermal strain
$h_{convection}$	Convective heat transfer coefficient (W/m^{2}K)
I	Current (Amperes)

NT11	Temperature (°C)
q	Power density (Wm^{-3})
Q	Total heat input (W)
R	Radial distance of the heat torch centre from the pipe axis (mm)
S, S22	Hoop residual stress (N)
S, S33	Axial residual stress (N)
t	Welding time (s)
T_{pipe}	Current pipe temperature (°C)
T_a	Ambien temperature (°C)
v	Welding speed (mm/s)
V	Voltage (volts)
Z	Axial direction starting from the WCL (mm)
2-D	Two-Dimensional
3-D	Three-Dimensional
A/D	Analog-to-digital converter
BM	Base material
CRA	Corrosion resistant alloy
C-Mn	Carbon-Manganese
FE	Finite element
FZ	Fusion zone
HAZ	Heat affected zone
TFP	Tight-fit-pipe
TIG	Tungsten Inert Gas
WCL	Weld centre line
WM	Welding material
θ	Angle of moving torch around the pipe (Rad)
μ	Welding efficiency (%)
σ_{bol}	Stefan-Boltzmann constant
σ_{em}	Effective radiation emissivity (($W/m^2 K^4$)
σ_v	Von Mises stress (Pa)

1. Introduction

Welding, in general, is a reliable process widely used in industry to join two specimens together with a high strength bond. In particular, oil and gas applications depend significantly on welding. Although it is a necessary process, the main problems of using lined pipe welding arise from the high temperatures at which two completely different filler materials are deposited into two different welding grooves, the weld overlay and girth welding grooves, which in turn lead to higher residual stresses concentrated in the two fusion zones (FZ) and heat affected zones (HAZ) [1]. Therefore, predicting the locations and magnitudes of residual stresses after completing the lined pipe welding operation is important to determine the reliability and integrity of welded structures. A lot of research work has been conducted to study the isothermal and residual stress fields induced by only single circumferential welding. Karlsson and Josefson [2] studied the effect of thermal field, residual stresses and radial shrinkage in a single-pass butt-welded C-Mn pipe (Carbon-Manganese) using 3-D FE models. To enhance the accuracy of the numerical solution in the welding process, Teng and

Chang [3] also developed 3-D FE models to study temperature and stress fields in carbon steel welded pipe with respect to the wall thickness variations. Deng and Murakawa [4] presented 2-D and 3-D FE models to validate the numerical thermal history and residual stress fields in multi-pass stainless steel pipe with experimental results. In their study, the results of both 2-D and 3-D models are consistent with the experimental results. Yaghi et al. [5] produced an axisymmetric thermomechanical FE model to predict the residual stresses in a circumferentially butt-welded P91 steel pipe. Moreover, the effect of phase transformation from austenite to martensite is considered in the simulation. Two methods were used to measure the residual stresses along the outer surface by means of X-ray diffraction and deep-hole drilling techniques. Dehaghi et al. [6] used an axisymmetric 2-D model to join a nozzle with a pipe in a power plant reactor due to complexity of welding processes, buttering and heat treatment,. It is pointed out that the buttering and heat treatment leads to reduce residual stresses in the nozzle and pipe, respectively.

A few research investigations have studied circumferential welding subjected to parametric factors. Brickstad and Josefson [7] used axisymmetric FE models to simulate multi-pass circumferential butt-welding of stainless steel pipe. In particular, the residual axial and hoop stresses across the wall thickness were discussed according to the variation in weld parameters, namely pipe size, heat input, weld metal yield stress and inter-pass temperature. The effect of the yield stress of the welding material on the residual stresses was investigated by Deng et al. [8]. Beyond the weld metal and its vicinity, significant discrepancies exist between the numerical and experimental results because of initial residual stresses produced by pre-heat treatment. Malik et al. [9] discussed the effect of welding speed on residual stresses. This study proves that a lower welding speed leads to a greater heat input. Consequently, the residual stresses increase because the FZ and HAZ become wider. The model developed by Zhao et al. [10] was used to study the effect of heat input and layer number on the residual stresses in a dissimilar butt-welded pipe where one pipe was made of austenitic stainless steel (S30432) and the other one was made of martensitic steel (T92). Their study states that a decrease in heat input would lower the tensile residual stresses in the S30432 steel more than those in the T92 steel. The possible reason is attributed to the yield stress which is much less in the S30432 steel than in the T92 steel. A 3-D FE numerical model was carried out by Velaga and Ravisankar [11] to study the effect of sixteen different geometrical conditions of heat source on welded austenitic stainless steel pipe. The results

point out that there is a slight effect on the temperature history and weld pool size whilst there is no considerable influence on residual stress distributions.

However, there are no detailed experimental or numerical studies conducted for lined pipe welding. Furthermore, no study has investigated the influence of different factors on lined pipe welding. Consequently, Obeid et al. [12] presented a new procedure to simulate a typical lined pipe process including the weld overlay and girth welding. Furthermore, a sensitivity analysis to determine the influence of the cooling time between weld overlay and girth welding and of the welding speed has been conducted thermally and mechanically.

In this study, six cases have been investigated by changing different factors affecting the quality and results of the welding process. Case A is considered the reference case, where the weld overlay and girth welding have accordingly been modelled with different materials for their base metals. In case B, the material of girth welding is the same material used in weld overlay, namely austenitic stainless steel. Case C considers the effect of neglecting the weld overlay where the two pieces of lined pipe have been joined solely using girth welding. In this case, the material of girth welding is the same used in case A. However, the weld overlay is used to seal the liner with the outer pipe which in turn blocks the gap between the liner and outer pipe at the pipe ends. The heat input plays a key role in the welding deformation and the residual stresses [13]. Therefore, in case D, the heat input is lowered to 75% of the heat input in case A for all welds. In a similar way, the heat input in case E is dropped to 50% of that in case A. The last case is case F where the liner with weld overlay is not considered.

To study the effect of specific parameters, the other parameters are kept constant and equal to the values of the reference case (case A). Furthermore, the mesh topology for all FE models remains with the same arrangement as in case A. The numerical thermal fields and residual stress distributions are compared against the experimental ones using thermocouples and residual stress gauges in all cases.

2. Manufacturing procedure

In this study, the specimen of welded lined pipe schematically shown in Fig. 1 was manufactured from two adjacent pipes. The outer pipe is made of low carbon steel equivalent to E235 AISI 10305-1, known as C-Mn pipe, with an outer diameter of 114.3 mm and a wall thickness of 6.35 mm. The inner pipe is made of austenitic stainless steel which is rich in Cr and Ni, known as AISI304 pipe, with an outer diameter of 101.6 mm and a wall thickness of 1.5 mm. The entire length of welded lined pipe, composed of two components, is 400 mm.

The AISI304 pipe was inserted inside the C-Mn pipe using tight fit pipe (TFP) thermal manufacturing process, which is based on heating the outer pipe and cooling down the inner one [14].

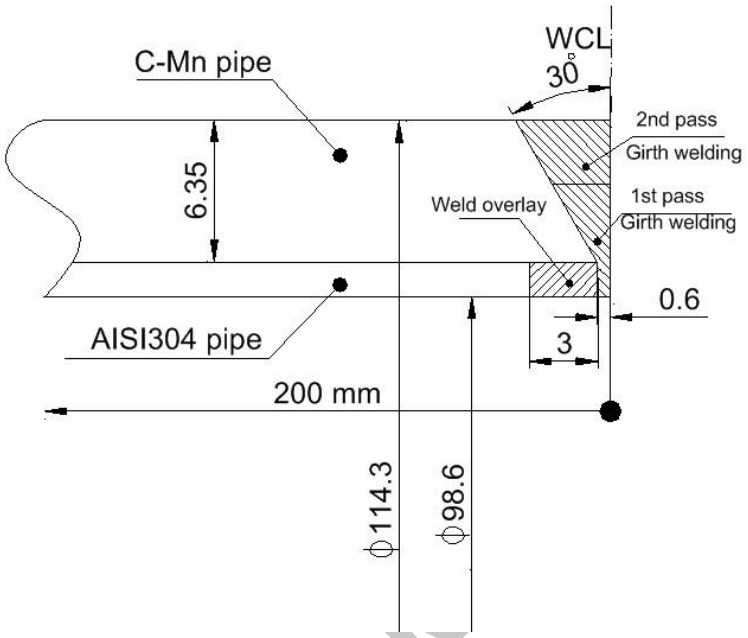

Fig. 1 Schematic semi-sketch of the welded lined pipe, dimensions in mm.

During welding, the heat source was fixed and the two sections of lined pipe were rotated with a uniform speed for each pass (one-pass weld overlay and two-pass girth welding). The weld overlay pass took 240 seconds to complete one revolution. Then, 270 seconds were consumed as inter-pass time between the weld overlay and girth welding to cool down the lined pipe naturally to the final maximum inter-pass temperature, which was around 100 °C. The first and second pass of girth welding required 270 seconds each, too. Also, there was a second inter-pass time between the two girth welding passes, again of 270 seconds. After the second girth welding pass, the entire lined pipe took 3000 seconds to finally cool down naturally to ambient temperature. In all passes, welding began at the central angle $\theta = 0°$ and then progressed through the anti-clockwise circumferential direction to complete one rotation and stop at the same starting point $\theta = 360°$. Tungsten Inert Gas (TIG) welding was used for all welds where ER308L stainless steel rod was inserted in the weld overlay groove whilst E70S2 mild steel rod was utilized to deposit the girth welding. Fig. 2 shows the lined pipe specimens during the welding overlay and girth welding.

(a) (b)

Fig. 2 Recording the temperatures during the (a) weld overlay and (b) girth welding

To record the thermal history, HI-766F K-type thermocouples, made of AISI 316 stainless steel, were placed at 6 axial locations with 270° central angle. The thermocouples can record temperatures up to 1100°C. The maximum accuracy of such thermocouple type is ±2.2°C. Three thermocouples were mounted on the outer surface (C-Mn pipe) and the others on the inner surface (AISI304) to record the thermal history at those locations during welding and cooling as shown in Fig. 3. The thermal history results were recorded and stored every 0.001 second by LabVIEW software via a 24-bit A/D interface (NI 9213). The maximum accuracy of the A/D interface is ±2.25°C. Consequently, the maximum error in the measured thermal history is the interval ±4.45°C.

To measure the residual stresses after completing welding and cooling down to ambient temperature, 14 residual stress gauges with three elements, FRS-2, were mounted also on the outer surface (C-Mn pipe) and the inner surface (AISI304). The tolerance of the gauge factor of the FRS-2 gauges is ±1% at room temperature. The residual stresses were also recorded every 0.001 second using LabVIEW software via a 24-bit A/D interface (NI 9235) with accuracy ±0.4%. Therefore, the error in the measured residual stress can reach a range of ±1.4%. A reference hole with diameter and depth of 2 mm each was drilled vertically through the pipe thickness using a high speed milling machine as shown in Fig. 4.

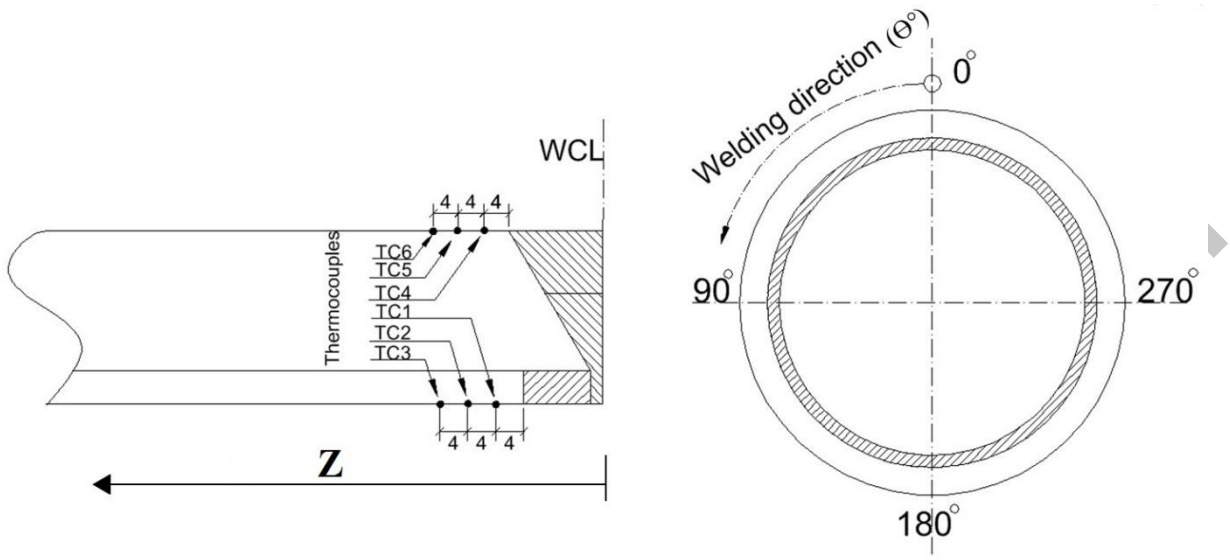

Fig. 3 Locations of thermocouples with the welding direction for three passes, dimensions in mm.

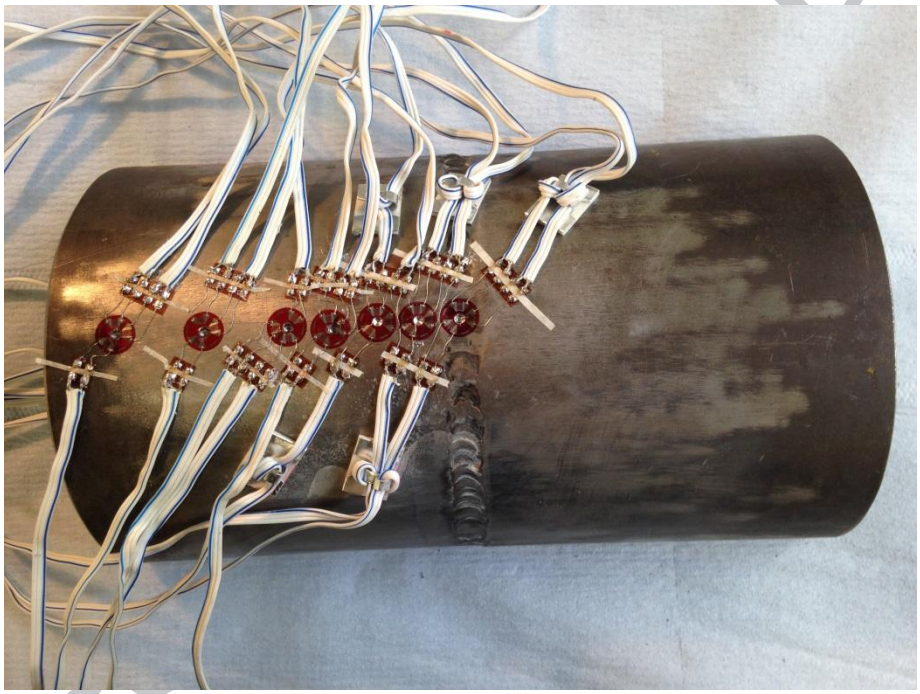

Fig. 4 Recording residual stress from rosette gauges, FRS-2.

3. Finite element modelling

In this study, all thermal and structural models have been executed using ABAQUS [15]. Due to the symmetry around the weld centreline, only one component, in particular, one-half of the welded lined pipe was modelled. It is clear that the mechanical properties in welding depend on the temperature whereas temperatures are assumed to be independent of mechanical deformation. Thus, the thermal analysis is simulated first to obtain the thermal history with respect to time for all nodes of the welded lined pipe. This thermal history is then accordingly transferred to the mechanical analysis as thermal loads.

In the thermal analysis, the element type is selected as a continuum, three-dimensional 20-node quadratic brick diffusive heat transfer element, named DC3D20 in ABAQUS. At each of its 20 nodes, there is one degree of freedom, which is the temperature. In the mechanical analysis, the element type is a continuum fully-integrated three-dimensional 20-noded element, named C3D20 in ABAQUS. Each of the 20 nodes undergoes three translation degrees of freedom to keep one element subjected to 60 degrees of freedom totally. Both the 3-D thermal and mechanical models have the same mesh associated with the same numbers and arrangements for nodes and elements as shown in Fig. 5. In the reference case (case A), the model consists of 35220 nodes associated with 7380 elements. Due to the high temperatures and their high gradients in the FZ and HAZ, a finer mesh can be seen in these regions of the weld overlay for the inner pipe, and of the two-pass girth welding for the outer pipe. The weld overlay, AISI304 pipe, girth welding and C-Mn pipe are coloured with red, light blue, yellow and green, respectively, as portrayed in Fig. 5.

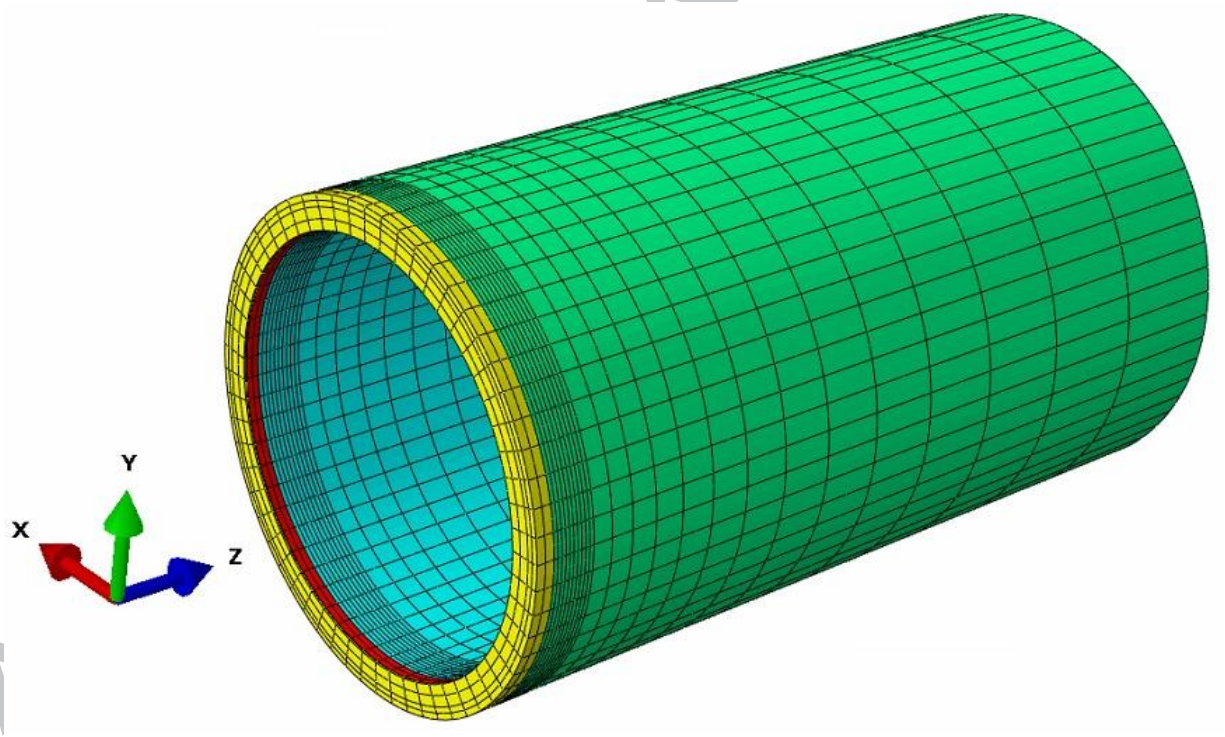

Fig. 5 3-D FE model (case A)

The element birth technique is adopted in the FE models to simulate the deposition of the filler materials in the weld overlay and girth welding grooves while moving the heat source.

In this study, both base and weld metals have the same thermal-mechanical material properties except the yield stress, where the weld material is supposed to have higher yield strength in both C-Mn and AISI304 as tabulated in Table 1 and Table 2, respectively.

Table 1 Thermo-mechanical properties of C-Mn [2].

Temperature (°C)	Density (Kg/m^3)	Specific heat (J/Kg K)	Conductivity (W/m K)	Thermal expansion ($x10^{-5}K^{-1}$)	Yield stress (MPa)		Young's modulus (GPa)	Poisson's ratio
					Base	Weld		
0	7860	444	50	1.28	349.45	445.42	210	0.26
100		480	48.5	1.28	331.14	441.29	200	0.28
200		503	47.5	1.30	308.00	416.49	200	0.29
300		518	45	1.36	275.00	376.18	200	0.31
400		555	40	1.40	233.00	325.54	170	0.32
600		592	35	1.52	119.00	172.59	56	0.36
800		695	27.5	1.56	60.00	43.41	30	0.41
1000		700	27	1.56	13.00	14.47	10	0.42
1200		700	27.5	1.56	8.00	9.30	10	0.42
1400		700	35	1.56	8.00	9.30	10	0.42
1600		700	122.5	1.56	8.00	9.30	10	0.42

Table 2 Thermo-mechanical properties of AISI304 [4].

Temperature (°C)	Density (kg/m^3)	Specific heat (J/kg K)	Conductivity (W/m K)	Thermal expansion ($x10^{-5}K^{-1}$)	Yield stress (MPa)		Young's modulus (GPa)	Poisson's ratio
					Base	Weld		
0	7900	462	14.6	1.70	265	438.37	198.50	0.294
100	7880	496	15.1	1.74	218	401.96	193	0.295
200	7830	512	16.1	1.80	186	381.5	185	0.301
300	7790	525	17.9	1.86	170	361.25	176	0.310
400	7750	540	18.0	1.91	155	345.94	167	0.318
600	7660	577	20.8	1.96	149	255.71	159	0.326
800	7560	604	23.9	2.02	91	97.41	151	0.333
1200	7370	676	32.2	2.07	25	28.41	60	0.339
1300	7320	692	33.7	2.11	21	16.23	20.00	0.342
1500	7320	700	120	2.16	10	12.17	10	0.388

The latent heat for C-Mn steel is set to be 247 kJ/kg between the solidus temperature of 1440 °C and the liquidus temperature of 1560 °C. For stainless steel (AISI304), the latent heat is assumed to be 260 kJ/kg between 1340 °C and 1390 °C, solidus and liquidus temperatures respectively. Consequently, the melting point for C-Mn is 1500 °C while it is 1365 °C for AISI304. The initial temperature of the lined pipe and the weld bead is set at room temperature.

3.1. Thermal Analysis

During welding, the heat transfer, a combination of heat loss due to radiation and convection, occurs upon external surfaces exposed to the environment. Radiation loss is dominating in the weld zone and its vicinity whereby the temperature magnitudes are near or over the melting temperature. Convection loss is dominating away from the weld zone. The Stefan-Boltzman law and Newton's law are applied to model the radiation and convection heat loss, respectively. In this work, the thermal boundary conditions are applied on all external

surfaces of the lined pipe. The total heat loss, q_{total}, is a combination of radiation, $q_{radiation}$, and convection, $q_{convection}$, losses given as follows:

$$q_{total} = q_{radiation} + q_{conviction} \quad (1)$$

$$q_{convection} = -h_{convection}(T_{pipe} - T_a) \quad (2)$$

$$q_{radiation} = -\sigma_{em}\varepsilon_{bol}(T_{pipe}^4 - T_a^4) \quad (3)$$

$$h_{total} = h_{convection} + \sigma_{em}\varepsilon_{bol}(T_{pipe} + T_a)(T_{pipe}^2 + T_a^2) \quad (4)$$

where $h_{convection}$ is the convective heat transfer coefficien, T_{pipe} is the current temperature at the pipe surface, T_a is the ambient temperature, σ_{em} is the effective radiation emissivity, ε_{bol} is the Stefan-Boltzmann constant and h_{total} is the total combined heat-transfer coefficient.

As the lined pipe is composed of two different materials, each material is characterised by different coefficients governing heat transfer with the room atmosphere, as shown in Table 3.

Table 3 heat transfer parameters

Parameters	C-Mn	AISI304
$h_{convection}$ (W/m^2 K)	8	5.7
σ_{em}	0.51	0.75
ε_{bol} (W/m^2 K^4)	5.67×10^{-8}	5.67×10^{-8}

A FILM user subroutine [15] has been coded in FORTRAN to implement in ABAQUS the above expression for the total heat-transfer coefficient, which is Eq. (4), for liner and outer pipe accordingly. It is worth noting that ABAQUS allows one single user-subroutine to be written for both materials by simply specifying which surface each condition applies to.

The power density, q, transmitted from the heat source to the lined pipe and weld regions is modelled by a Gaussian distribution as a function of position and time, t, in an ellipsoid (welding pool) with centre that is taken as (x_0, y_0, z_0) [12]:

$$q(x,y,z,t) = \frac{6Q\sqrt{3}}{abc\pi\sqrt{\pi}} e^{-3(x-(R\sin\theta+x_0))^2/a^2} e^{-3(y-(R\cos\theta+y_0))^2/b^2} e^{-3(z-z_0)^2/c^2} \quad (5)$$

where $Q = IV\mu$ is the energy input rate which is given by the product of the current I, voltage V and the weld efficiency μ, R is the radial distance of the heat torch centre from the pipe axis, θ is the angle from the start/stop point (where θ = 0°). Welding parameters a, b and c are the semi-axes of the ellipsoidal welding pool in directions, x, y and z, respectively. Equation (5) has been implemented in ABAQUS by coding the DFLUX user-subroutine. The position of the weld torch is calculated first in DFLUX according to the welding time t. Thereafter, the power density, q, is computed at each integration point.

The numerical values for the variables used in the power density distribution in Eq. (5) are illustrated in Table 4 for each welding material.

Table 4 Heat source and welding parameters.

Parameter	Symbol	Weld overlay	1st pass girth welding	2nd pass girth welding
Half-length of arc (mm)	a	4.9	6.2	6.2
Depth of arc (mm)	b	1.5	2.62	2.85
Half-width of arc (mm)	c	4.9	5.57	5.66
Welding current (A)	I	110	220	234
Voltage (V)	V	22	22	22
Welding speed (mm/s)	v	1.3	1.26	1.33
Welding time (s)	t	240	270	270
Welding efficiency	μ	70%	70%	70%

3.2. Structural analysis

The same FE mesh used in the thermal analysis is employed in the mechanical analysis apart from the boundary conditions and element type. Herein, the nodal temperature histories read from the thermal output file are considered thermal loads for each increment in the mechanical simulation. At each structural step, an automatic time increment is executed and geometrical nonlinear effects (large deformation) have been incorporated in the FE model.

During the lined pipe welding process, the effects of volumetric change and the change in the yield stress value (the transformation plasticity) due to the metallurgical phase transformation, namely the martensitic phase transformation, have been neglected in this work because the volume dilation [16] and the reduction in the yield stress value [5] due to the phase transformation is small. Therefore, the increment of the total strain, $d\varepsilon_{ij}$, has been broken down into three components as follows [12]:

$$d\varepsilon_{ij} = d\varepsilon_{ij}^{e} + d\varepsilon_{ij}^{p} + d\varepsilon_{ij}^{th} \tag{6}$$

where $d\varepsilon_{ij}^{e}$, $d\varepsilon_{ij}^{p}$ and $d\varepsilon_{ij}^{th}$ are the elastic, plastic and thermal strain increment, respectively. The elastic behaviour is defined by the isotropic Hook's law. For the plastic behaviour, the Von Mises, σ_v, yield criterion has been used with an associated flow rule with respect to the three principal stresses, σ_1, σ_2 and σ_3, given as below [10]:

$$\sigma_v = \sqrt{\frac{1}{2}[(\sigma_1 - \sigma_2)^2 + (\sigma_2 - \sigma_3)^2 + (\sigma_3 - \sigma_1)^2]} \tag{7}$$

The thermal strain is the result of expansion and contraction of the line pipe materials and is governed by the temperature-dependant thermal expansion coefficient reported in Tables 1 and 2.

The Bauschinger effect should be taken into account in the structural analysis because all material nodes are under the influence of multiple thermal loading and unloading. In the kinematic hardening rule, the Bauschinger effect considers that the size and shape of the yield surface keep the same with translating in the stress space. Consequently, a linear kinematic hardening rule has been assumed for both materials C-Mn and AISI304 [12], with the hardening parameter obtained from the temperature-dependant yield stress reported in Fig. 6, when the plastic strain of C-Mn [9] and AISI304 [8] is equal to 1%.

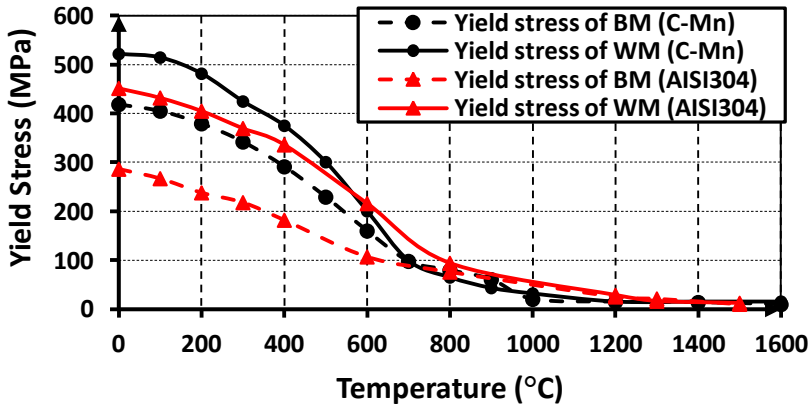

Fig. 6 Yield stress of the base material (BM) and welding material (WM) for C-Mn steel [9] and AISI304 [8] corresponding to 1% hardening.

The mechanical boundary conditions are applied to restrict the axial movement on the circumferential symmetry-plane. As the lined pipe is not clamped during welding, lateral and transversal restrictions are employed at the lined pipe end to prevent rigid body motion whereas the free expansion and contraction are allowed over the entire lined pipe.

4. Results and discussion

4.1. Temperature response in case A

Incorporating the heat source movement within the heat transfer analysis during welding is complicated by mathematical and physical issues, because of the need to consider two different types of welding (weld overlay and girth welding) associated with two different parent materials at the same time. It is important to validate the FE model experimentally to verify the accuracy of the moving heat source and heat transfer equations. The macrograph of cross section at 270° in case A has been taken by means of a microscope where the FZ and

HAZ boundaries are clearly distinct as shown in Fig. 7. From this figure, it can also be seen that the predicted FZ and HAZ isotherms correlate well with the crystallization of the lined pipe cross section. The minimum temperature at the FZ is 1365 °C and 1500 °C for weld overlay and girth welding, respectively. The HAZ extends in the FZ vicinity to attain a minimum temperature of 800 °C.

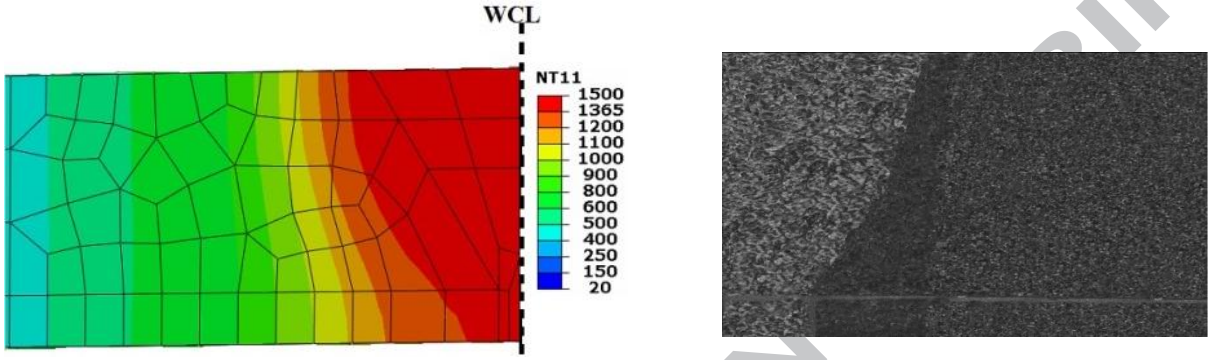

Fig. 7 The numerical FZ and HAZ isotherms and macroscopic examination at the cross section of 270° central angle (case A).

Consequently, the macroscopic examination and numerical results of FZ and HAZ isotherms prove that the accuracy is not only in the thermal equations used in this work but also in the parameters applied to these equations such as welding pool geometries and heat input values.

For typical welding, temperatures in the fusion zones of weld overlay and two-pass girth welding should be higher than the melting points, 1500 and 1365 °C for C-Mn and AISI304, respectively, to make filler materials flow through the grooves. Moreover, all points located on the same circumferential direction should have an identical temperature history.

Fig. 8 shows the numerically computed temperature distributions at 90°, 180° and 270° central angle during weld overlay where the girth welding has not been deposited yet in case A. As anticipated, the maximum temperature is achieved at the welding pool centre of weld overlay, 1634°C, which is beyond the melting point of AISI304, 1500 °C. From this figure, it can be seen that the thermal histories of weld overlay pool centres at three circumferential locations, 90°, 180° and 270, have to a reasonable extent the same shape and magnitudes of the transient thermal cycle.

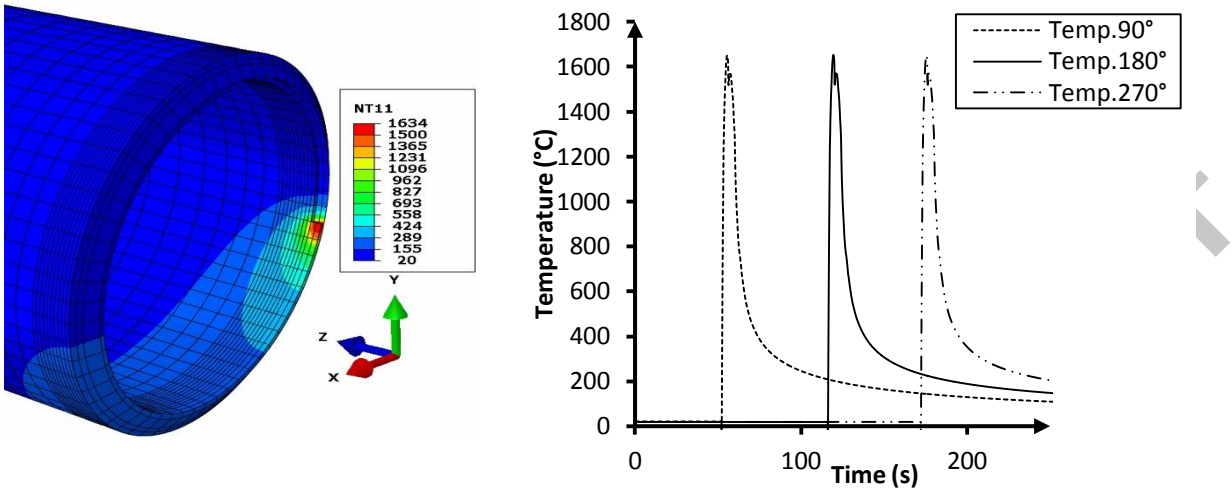

Fig. 8 The thermal history (°C) of weld overlay centre at 90°, 180° and 270° central angle (case A).

Likewise, the numerically computed temperature history at the second pass of girth welding also has identical distributions circumferentially around the mid-plane (symmetric line) at three locations, 90°, 180° and 270° in case A. The three curves reach the same peak temperature, 2076°C, and it could be seen that the weld overlay and first-pass girth welding and three quarters of the second-pass girth welding have been laid down in their grooves as shown in Fig. 9.

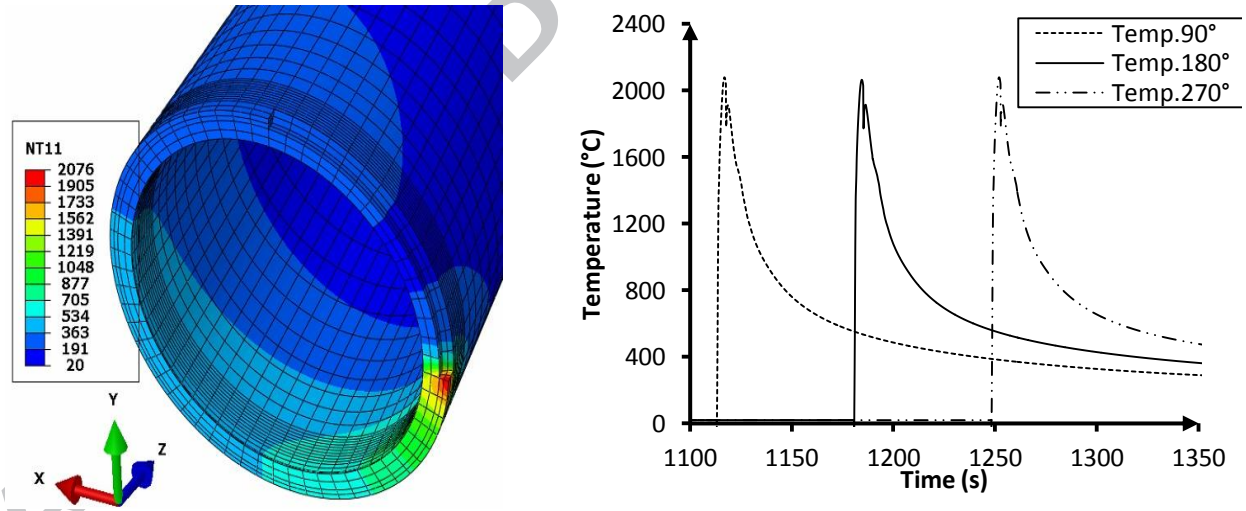

Fig. 9 The thermal history (°C) of second pass centre of girth welding at 90°, 180° and 270° central angle (case A).

4.2. Comparisons of thermal results

To compare the thermal results of the reference case (case A) with other cases, Table. 5 shows the peak temperatures at the six thermocouples during the weld overlay, the first and second pass of girth welding. The numerical temperature gradients are compared with the results recorded experimentally.

Table 5 Comparison between numerical and experimental results at six location during welding

Case	Pass		Inner surface °C			Outer surface °C		
			TC1	TC2	TC3	TC4	TC5	TC6
A	Overlay	Num.	540	350	271	446	342	271
		Exp.	525	343	265	432	333	263
	1-Girth	Num.	798	565	450	709	554	448
		Exp.	775	550	441	695	540	435
	2-Girth	Num.	929	703	573	918	690	570
		Exp.	913	685	562	910	681	558
B	Overlay	Num.	538	348	271	446	341	271
		Exp.	525	331	260	430	332	264
	1-Girth	Num.	790	564	450	708	554	448
		Exp.	775	552	443	690	539	441
	2-Girth	Num.	928	704	574	911	692	570
		Exp.	911	685	561	895	680	561
C	Overlay	Num.	-	-	-	-	-	-
		Exp.	-	-	-	-	-	-
	1-Girth	Num.	689	482	374	614	472	374
		Exp.	670	471	362	605	460	361
	2-Girth	Num.	894	669	539	878	658	537
		Exp.	882	650	525	865	645	525
D	Overlay	Num.	408	271	212	345	268	212
		Exp.	401	265	208	337	262	208
	1-Girth	Num.	610	440	352	552	432	353
		Exp.	600	431	340	540	422	339
	2-Girth	Num.	716	553	453	701	548	453
		Exp.	701	542	438	688	535	451
E	Overlay	Num.	276	191	151	240	188	151
		Exp.	270	185	145	232	179	142
	1-Girth	Num.	412	306	248	388	302	248
		Exp.	405	301	245	375	295	235
	2-Girth	Num.	496	387	320	492	386	320
		Exp.	485	375	315	485	378	315
F	Overlay	Num.	-	-	-	-	-	-
		Exp.	-	-	-	-	-	-
	1-Girth	Num.	730	531	417	610	475	374
		Exp.	721	520	412	600	461	362
	2-Girth	Num.	1010	744	599	875	655	535
		Exp.	992	732	585	861	645	526

Comparing the thermal results of case A against case B, it can be observed that the peak temperatures for all points are close to each other with differences of less than 10 °C at all points. Consequently, changing the girth welding material to austenitic stainless steel does not influence the thermal results during welding. This can be attributed to the thermal properties, namely the specific heat and conductivity, which are close to each other especially at high temperatures.

In case C, the differences in temperatures measured by thermocouples drop drastically compared with case A during the first pass of girth welding because the inter-pass

temperature is neglected in case C. In the second pass of girth welding, the variations in temperatures between two cases are significantly narrower.

Decreasing the heat input from the heat source leads to a strong decrease in temperatures during all welding passes. In more detail, the maximum temperatures predicted and recorded by thermocouples in cases D and E are significantly lower than their counterparts in case A. Furthermore, temperatures in case D are larger than those in case E because case D has 75% of case A heat input, whilst case E just has 50%.

Removing the liner and weld overlay in case F keeps the whole thickness minimized to that of the C-Mn pipe, equal to t = 6.35 mm. In this case, it can be seen that the peak temperatures recorded and predicted at each thermocouple during the first girth welding pass are lower than their counterparts in case A because the inter-pass temperature is not there anymore. During the second pass of girth welding, the temperatures in case F are higher than those in case A on the inner surface where the thickness of pipe is 6.35 mm. On the outer surfaces, the temperatures are much closer to their counterparts in case C.

It can be observed that there is good agreement between the numerical and experimental temperatures which are within a maximum variation of less than 6%. Thus, the developed thermal FE models for all cases can be considered to be validated experimentally. Also, the disparity between the results of case A and other cases becomes larger as the distance from the WCL decreases. It is also observed from Table 5 that the thermocouple on either the outer or inner surface located nearest to the WCL experiences a peak temperature higher than those located farther from the WCL [17].

4.3. Structural response in case A

In case A, the axial and hoop residual stress distributions at 270° central angle are depicted in Fig. 10(a) and (b), respectively. The bottom row of elements is the liner, AISI304 pipe, with the weld overlay, whereas the rest of pipe is the backing steel pipe, namely C-Mn pipe, with the girth welding.

It can be seen that maximum axial residual tensile stresses are located at the toes of the girth welding, weld overlay and HAZ on the inner surface as shown in Fig. 10(a). Furthermore, the axial tensile stresses on the inner surface are balanced by the axial compressive stresses on the FZ and HAZ of girth welding on the outer surface [18]. Therefore, axial bending deformation is produced through the pipe cross section. As a result, the diameter of lined pipe becomes smaller in the FZ and HAZ regions after cooling down to room temperature because

of radial shrinkage [19]. Also, it can be seen that the length needed to reverse the tensile stresses to compressive on the inner surface is narrower than that to reverse the compressive stresses to tensile on the outer surface.

Turning to the hoop residual stress distributions shown in Fig. 10(b), the absolute values of tensile stresses in the FZ and HAZ on the inner surface are significantly larger than those of the compressive stresses in the girth welding region and its vicinity on the outer surface. The magnitudes of residual axial stresses have a significant influence on the value of residual hoop stresses [20]. The ranges of reversal stresses on the inner and outer surface are somewhat close to each other.

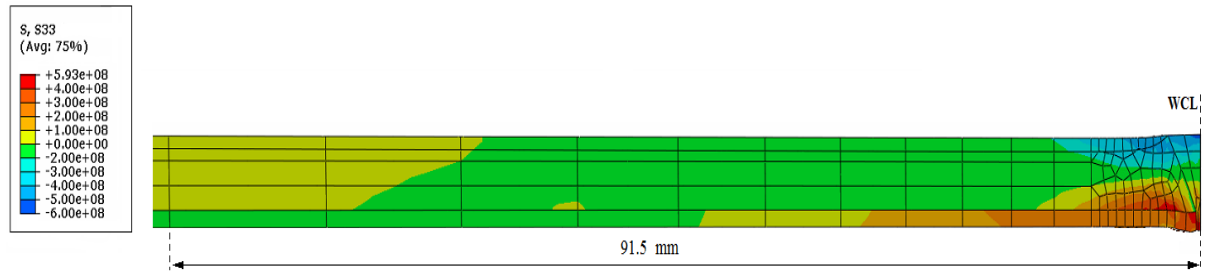

(a)

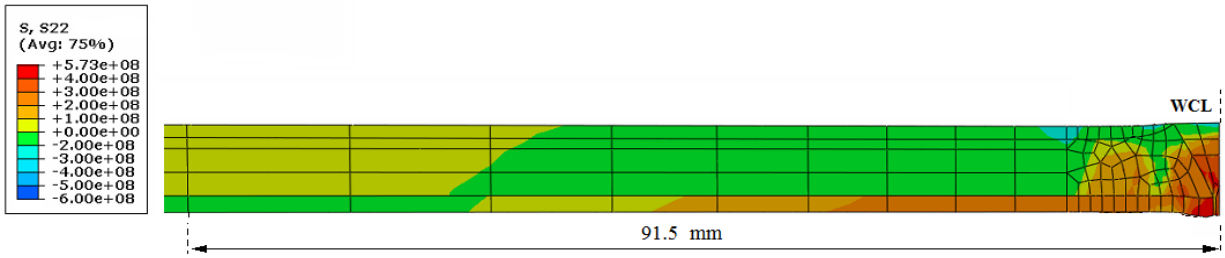

(b)

Fig. 10 (a) Axial and (b) hoop residual stress distributions of case A at 270° central angle.

It is evident that the area of C-Mn steel at which the weld overlay is fixed with the C-Mn pipe has relatively higher axial and hoop tensile residual stresses which result in von Mises stresses larger than the yield stress of the C-Mn base material. This region is affected more than others by the thermal cycles of weld overlay, first pass and second pass of girth welding. Consequently, it is more likely that a crack initiates at this area as shown in Fig. 11.

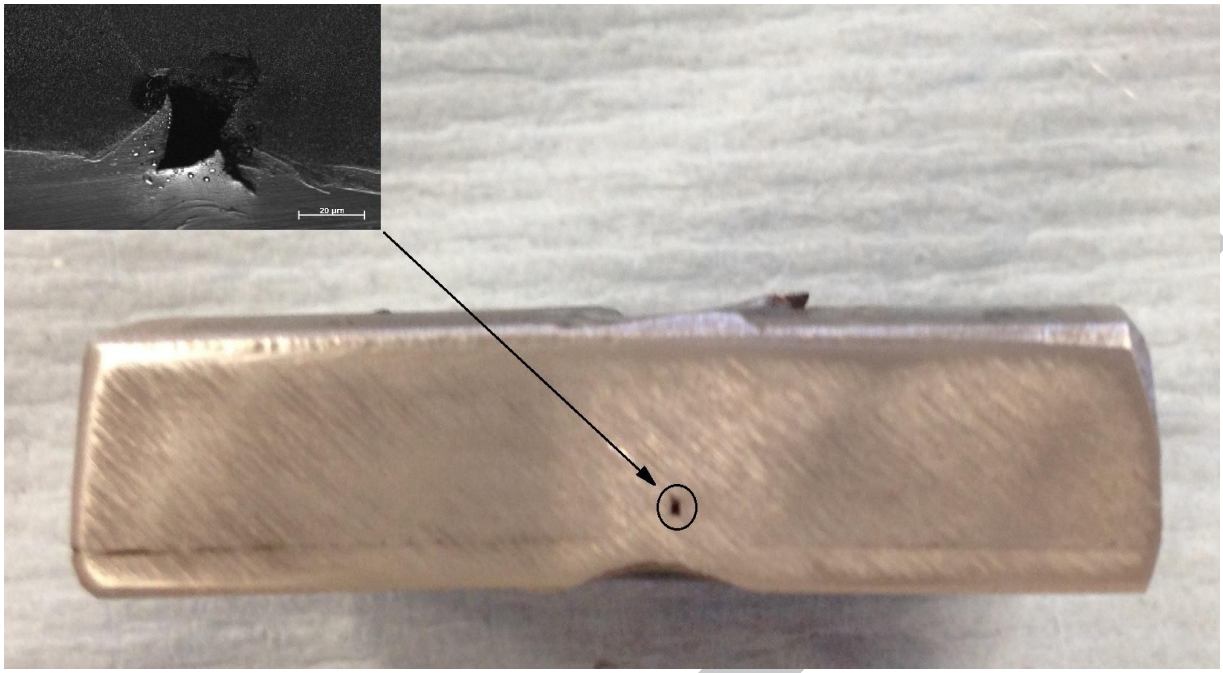

Fig. 11 Initiation and growth of crack at the area of C-Mn pipe above weld overlay.

4.4. Comparison of structural results

4.4.1. Effect of welding materials on residual stresses

To avoid cracking and corrosion in the FZ, austenitic stainless steel is a proper filler material to join two specimens together. Stainless steel is more capable of expanding and contracting naturally during welding because of its larger coefficient of thermal expansion. Conversely, carbon steel is a good conductor of heat which in turn cools more rapidly and shrinks faster as the joint cools [21]. Moreover, stainless steel has a better corrosion resistance than carbon steel because of its chemical composition. As a result, austenitic stainless steel welding is preferred in the oil and gas industries.

Fig. 12(a)-(d) shows a comparison between the numerical results for cases A and B at 270° central angle from the start/stop welding point along the axial direction starting from the WCL, Z=0. The experimental results are also plotted for both cases accordingly using residual stress gauges. The numerical axial and hoop residual stress distributions on the inner surface (liner) for both cases are in a good correlation except at the toes of weld overlay and girth welding ($Z \leq 3.6$ mm). Within this zone, the maximum axial residual stress is 593 MPa at Z = 0.3 mm in case A whilst the maximum one in case B is 529 MPa located at Z = 0.6 mm as shown in Fig. 12(a). Similarly, in the circumferential direction, the maximum hoop residual stress is 573 MPa, over the yield stress of AISI304 welding material, at Z = 2.1 mm in case A whereas the maximum one in case B is 481 MPa on the WCL as indicated in Fig. 12(b). On the outer surface, it can be seen that significant discrepancies exist between the

numerical results of case A and B in the FZ and its vicinity, for $Z \leq 45$ mm, as shown in Fig. 12(c) and (d). Beyond this zone, the results in both cases are almost identical in the axial and hoop residual stress distributions.

The experimental results recorded on the inner and outer surface with 270° central angle are consistent with the numerical results in the FZ and HAZ because the initial residual stresses produced by the manufacturing process (TFP) are removed by the high temperatures of welding. Beyond this range, numerical temperature magnitudes are significantly lower. As a result, the initial stresses still remain in the pipe and the experimental results are somewhat larger.

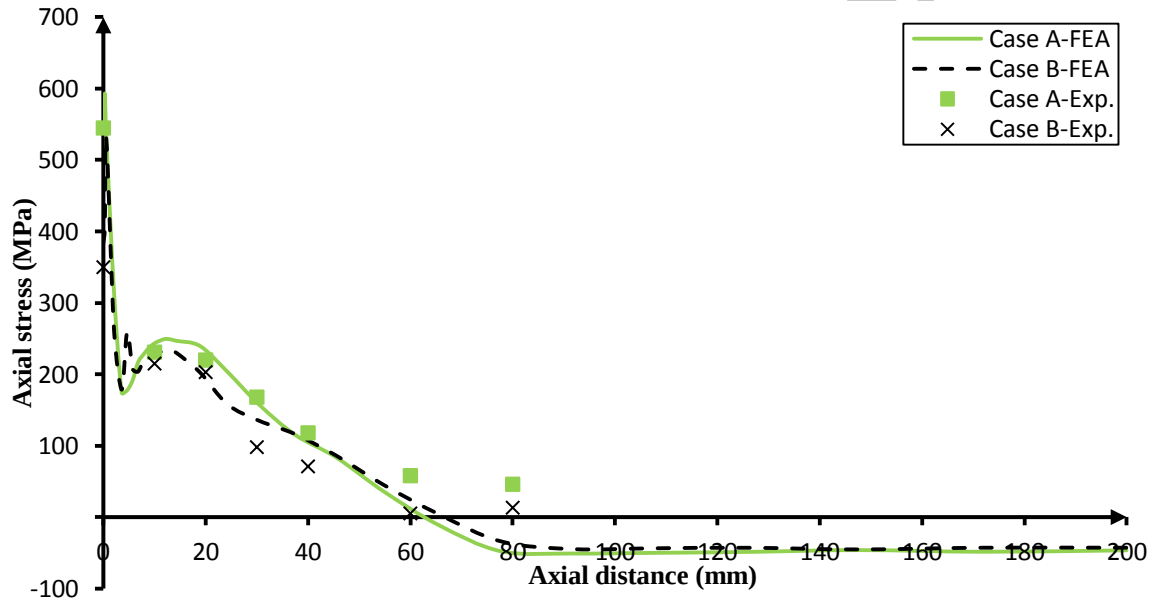

(a)

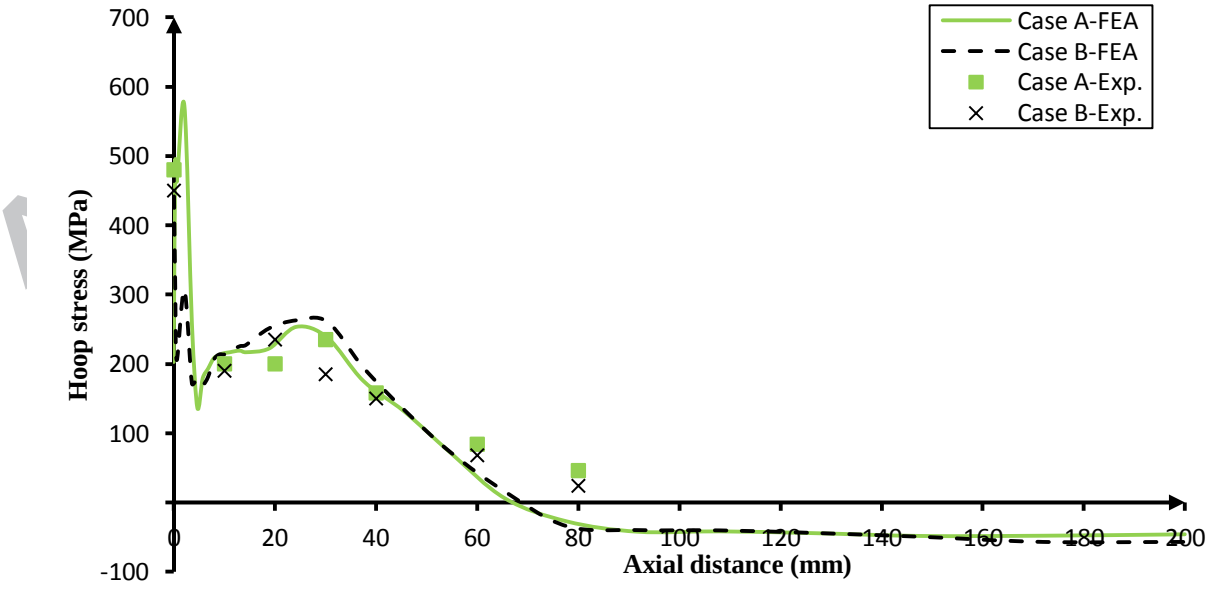

(b)

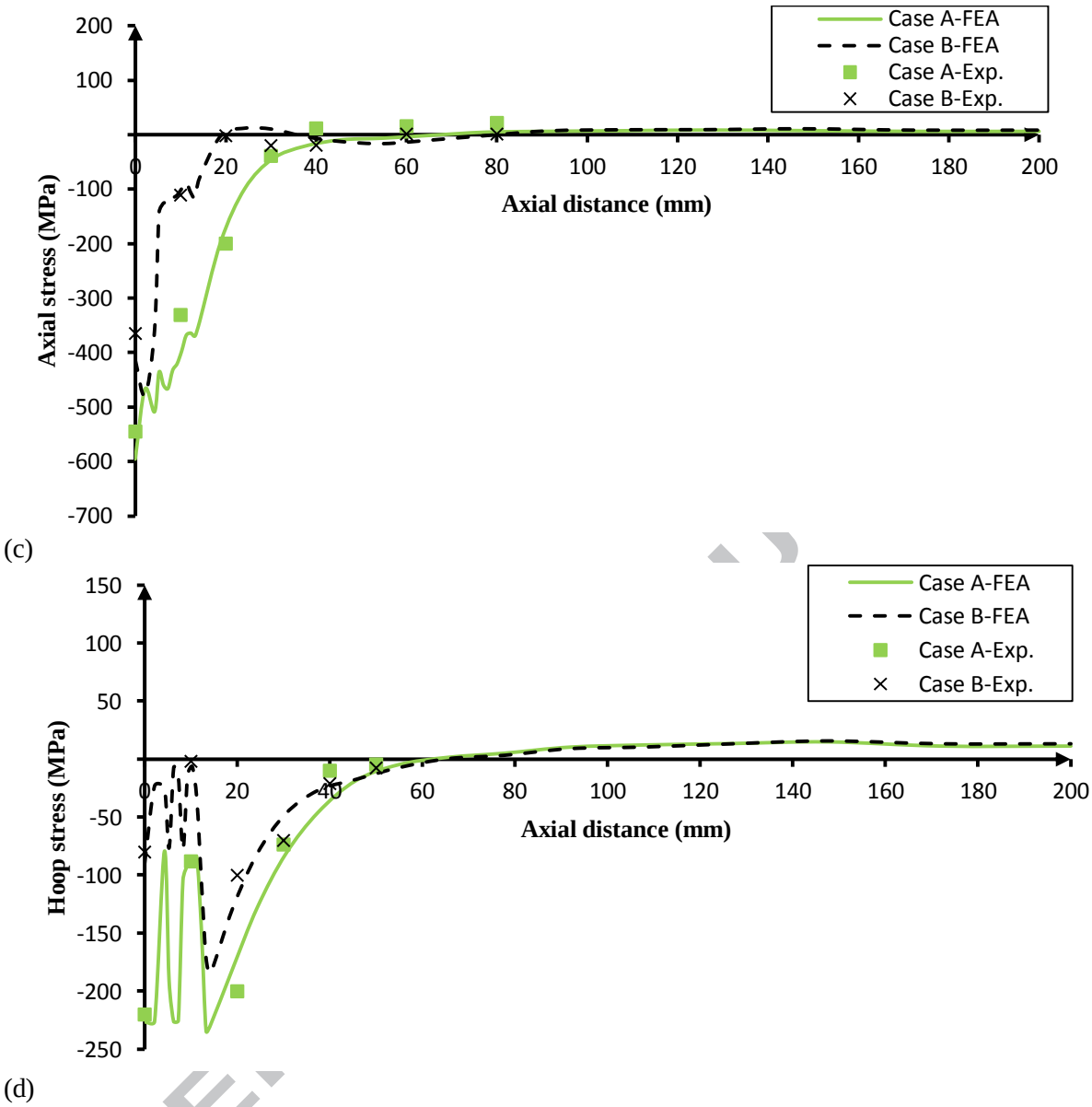

Fig. 12 Comparison of residual stresses at 270° central angle between case A and case B: (a) axial stress distributions on the inner surface, (b) hoop stress distributions on the inner surface, (c) axial stress distributions on the outer surface, and (d) hoop stress distributions on the outer surface.

4.4.2. Effect of welding overlay

Omitting the weld overlay allows dust and grease to go inside the gap between the liner and backing steel pipe. Consequently, these go inside the girth welding and deteriorate the quality of girth welding by forming voids and inclusions. Therefore, in case C welding is conducted without weld overlay to study the influence of this factor on the stress behaviour.

Fig. 13(a)-(d) shows the hoop and axial residual stress distributions at 270° central angle on the inner and outer surfaces for cases A and C. In this figure, the experimental results are also plotted along the axial distance. It can be observed that there is a significant discrepancy in the axial residual stress at the WCL where it is 540 MPa and 252 MPa in case A and C,

respectively. Beyond these weld zones, the axial residual stress distributions in both cases A and C are much closer to each other as shown in Fig. 13(a). Similarly, in the hoop direction, there is a difference in the hoop residual stress at the weld zones. Beyond that, the results are closer to each other in both cases as depicted in Fig. 13(b).

On the outer surface, there are significant discrepancies between the results of axial and hoop residual stress in case A with their counterparts in case C at the weld zone of girth welding and its HAZ as shown in Fig. 13(c)-(d). The experimental results are in good agreement with the numerical results for both cases at the FZ and HAZ but they are larger beyond that especially at the inner surface due to the effect of initial residual stresses of pre-heat treatment (TFP).

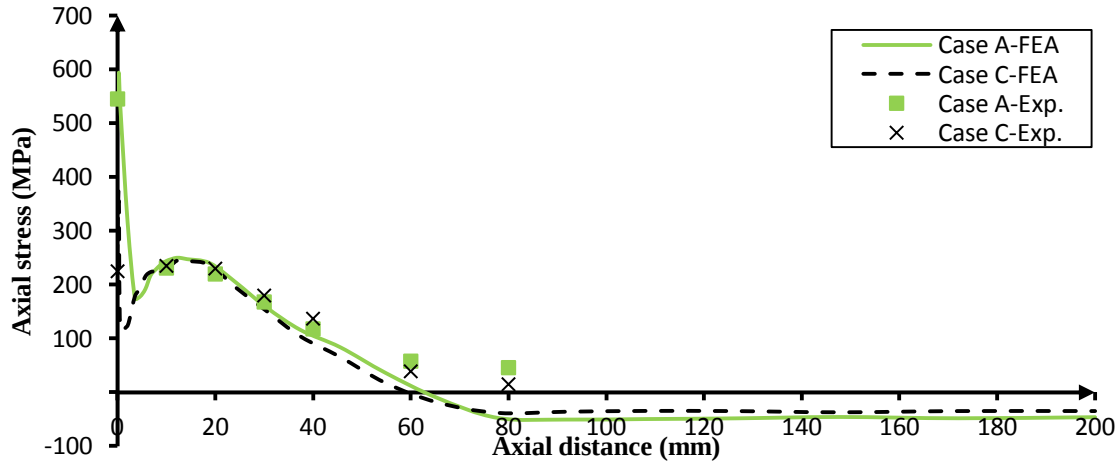

(a)

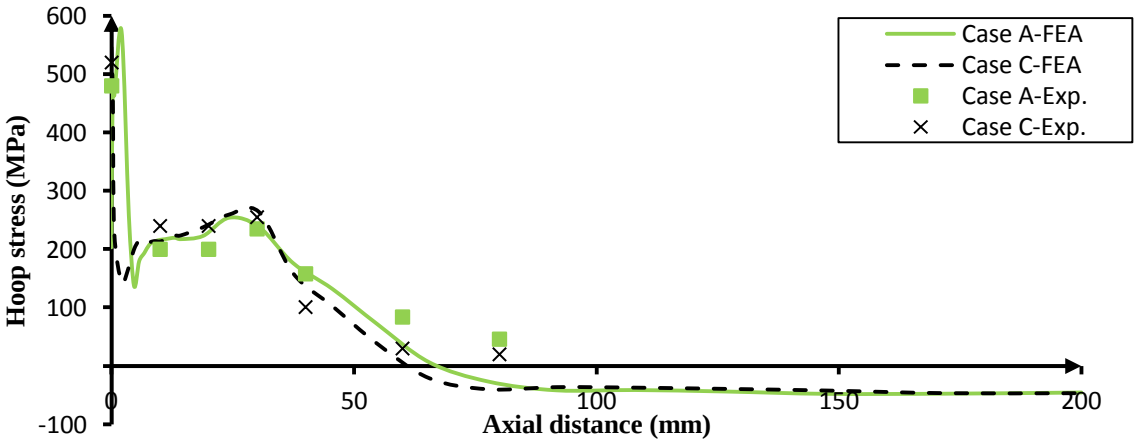

(b)

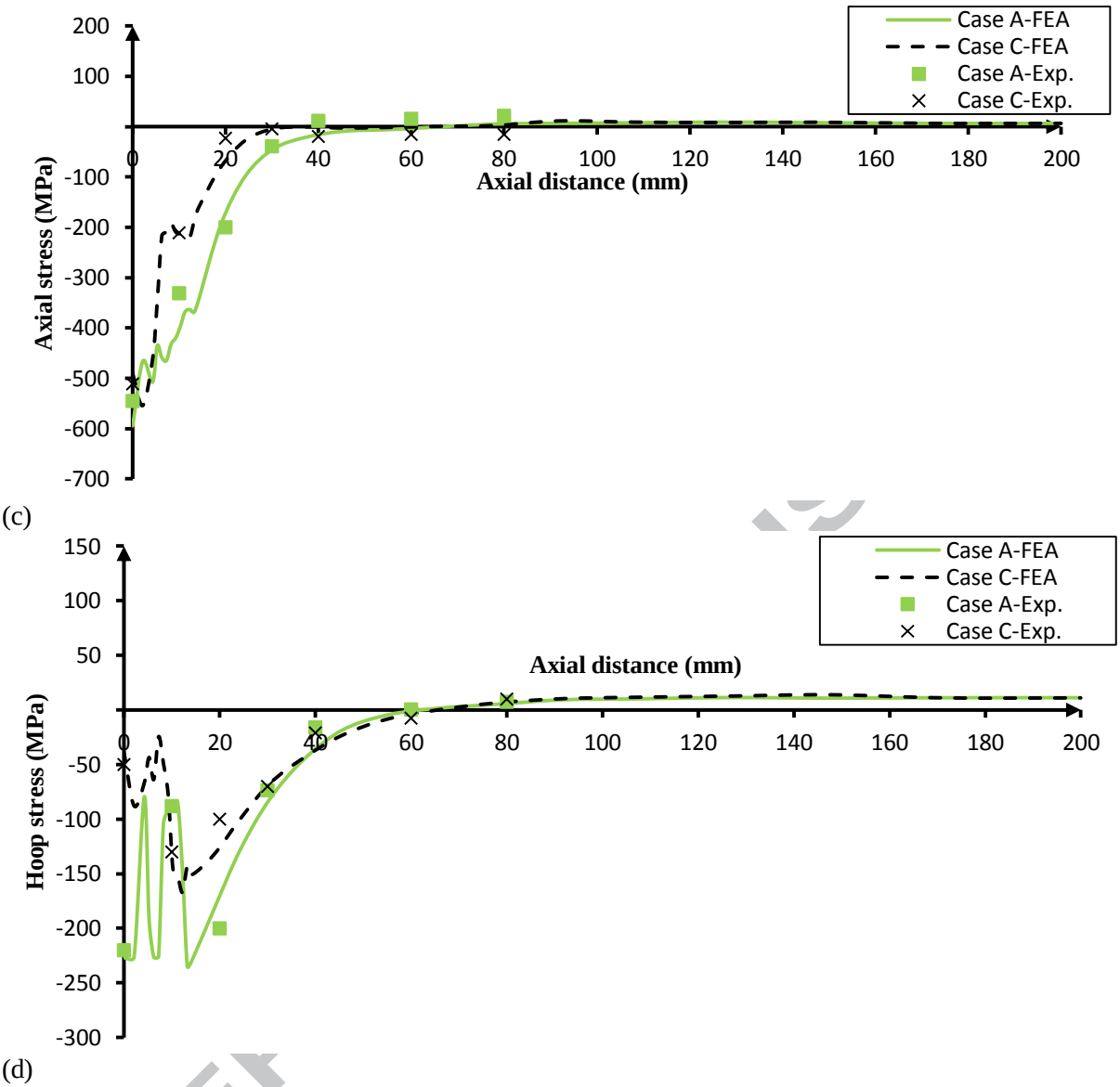

Fig. 13 Comparison of residual stresses at 270° central angle between case A and case C: (a) axial stress distributions on the inner surface, (b) hoop stress distributions on the inner surface, (c) axial stress distributions on the outer surface, and (d) hoop stress distributions on the outer surface. and (d) hoop stress distributions on the outer surface.

4.4.3. Effect of heat input on welding residual stress

The heat input plays a key role in affecting the temperature distributions, which in turn leads to significant changes in residual stresses. In this section, all welding parameters are kept constant, such as the welding speed and welding pool geometries. The total heat input, Q, is identified as $Q = IV\mu$ (Watts) where I is current (Amps), V is voltage (Volts) and μ is the weld efficiency. In case A, the total heat inputs are 850, 1700 and 1800 Watts for weld overlay, first-pass of girth welding and second-pass of girth welding, respectively. Reducing the heat input has some benefits in reducing consumption of the rod in TIG welding provided the quality of welding is achieved without porosity (bubbles) in the weld because of the lack

of fusion. In this section, the influence of heat input on residual stresses has been investigated through cases D and E. The total heat input is lowered to 0.75 and 0.5 of the heat input of case A for case D and E, respectively. In more detail, the total heat inputs become 638, 1275 and 1350 Watts for weld overlay, first-pass of girth welding and second-pass of girth welding in case D, respectively. In case E, the portions of heat input which have been provided to the weld overlay, first-pass of girth welding and second-pass of girth welding are 425, 850 and 900 Watts, respectively.

Fig. 14(a)-(d) compares the axial and hoop residual stresses from the numerical analysis with experimental data in the longitudinal direction starting from the WCL at 270° from the start/stop welding location for cases A, D and E. On the inner surface (AISI304 pipe), the maximum axial residual stresses in the three cases are located at Z = 0.3 mm at the toe of girth welding with values of 590, 577 and 352 MPa for cases A, D and E, respectively, as shown in Fig. 14(a). Turning to the hoop direction, it can be seen that the maximum tensile hoop residual stresses in cases A, D and E take place at the centre of the weld overlay region, Z = 2.1 mm, with values of 573, 371 and 502 MPa as shown in Fig. 14(b), respectively. From Fig. 14(a) and (b), it is observed that the length of the zone with tensile residual stress becomes narrower by reducing the magnitude of the heat input.

Fig. 14(c) and (d) depicts the axial and hoop residual stress distributions on the outer surface (C-Mn pipe) for cases A, D and E at 270° central angle with respect to the axial distance. The maximum axial compressive stresses on the outer surface are located at the WCL with -595, -561 and -508 MPa for the three cases A, D and E, respectively. The lengths of the zones with compressive residual stress are slightly close to each other where the zone for case E is still narrower than others as indicated in Fig. 14(c). It is observed that the magnitude of hoop residual stress on the outer surface is affected by its axial residual stresses. The larger the compressive axial residual stress is, the larger the compressive hoop residual stress is [22]. In a similar way, case E has the narrowest compressive range of all the cases, as shown in Fig. 14(d). Experimental results are in good agreement with their counterparts from numerical analysis in the FZ and HAZ for all cases.

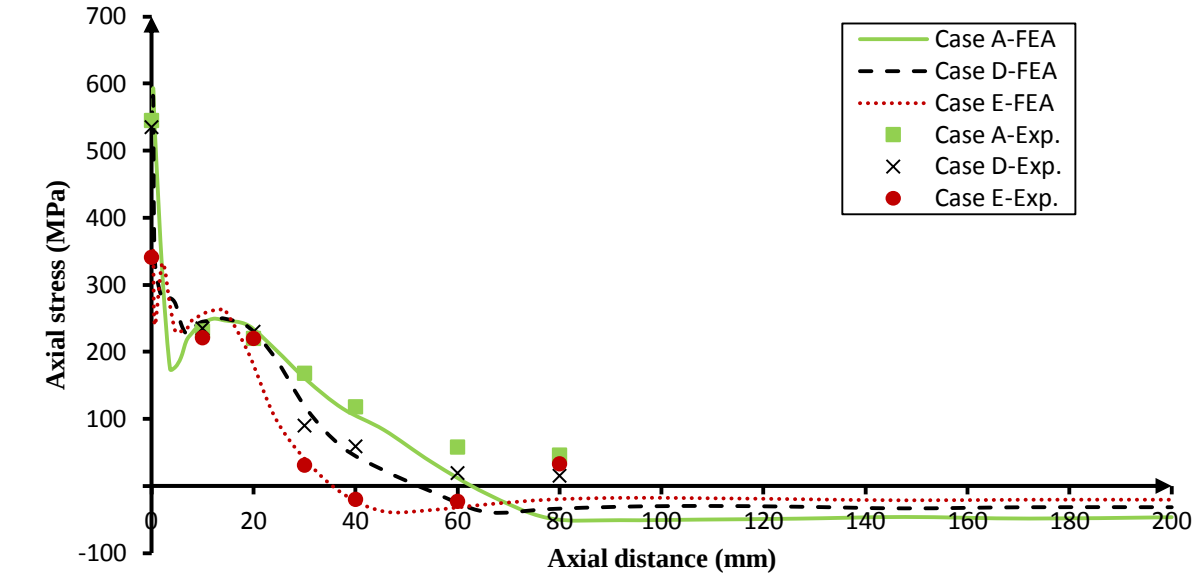

(a)

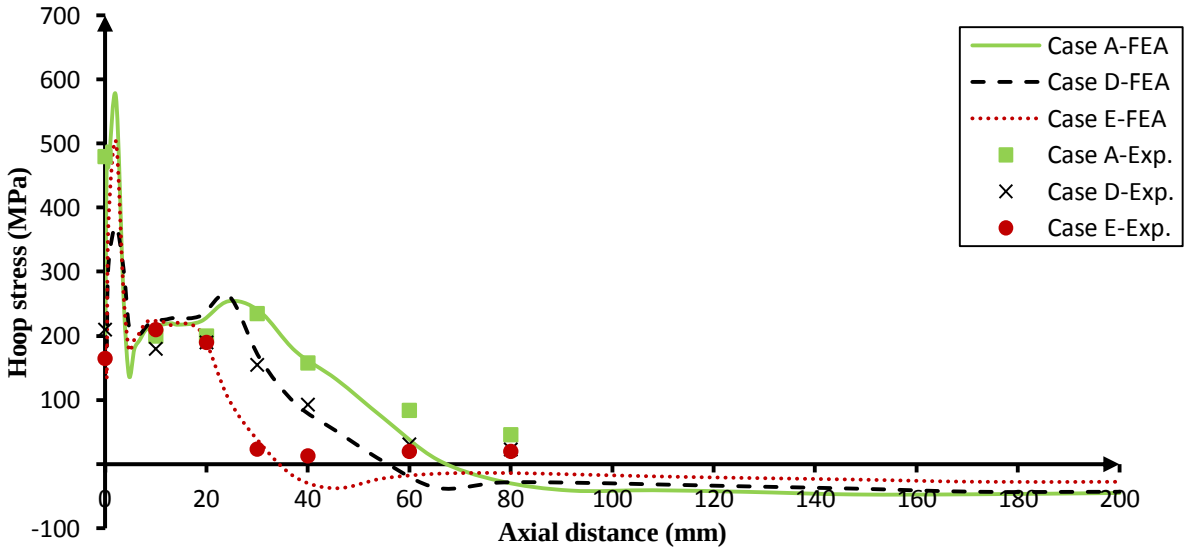

(b)

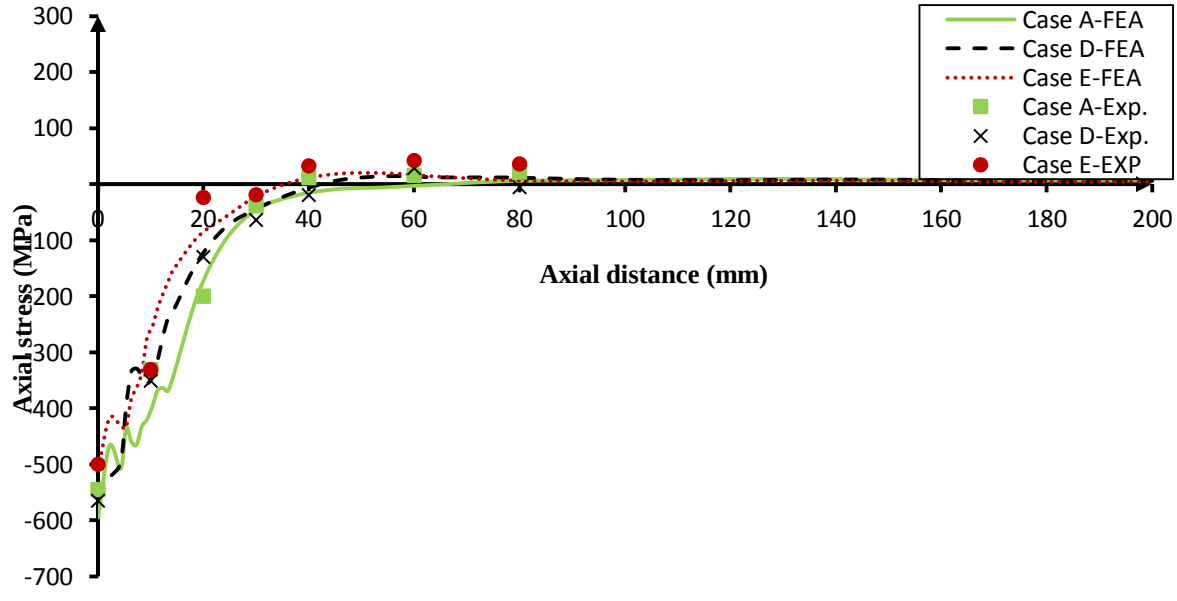

(c)

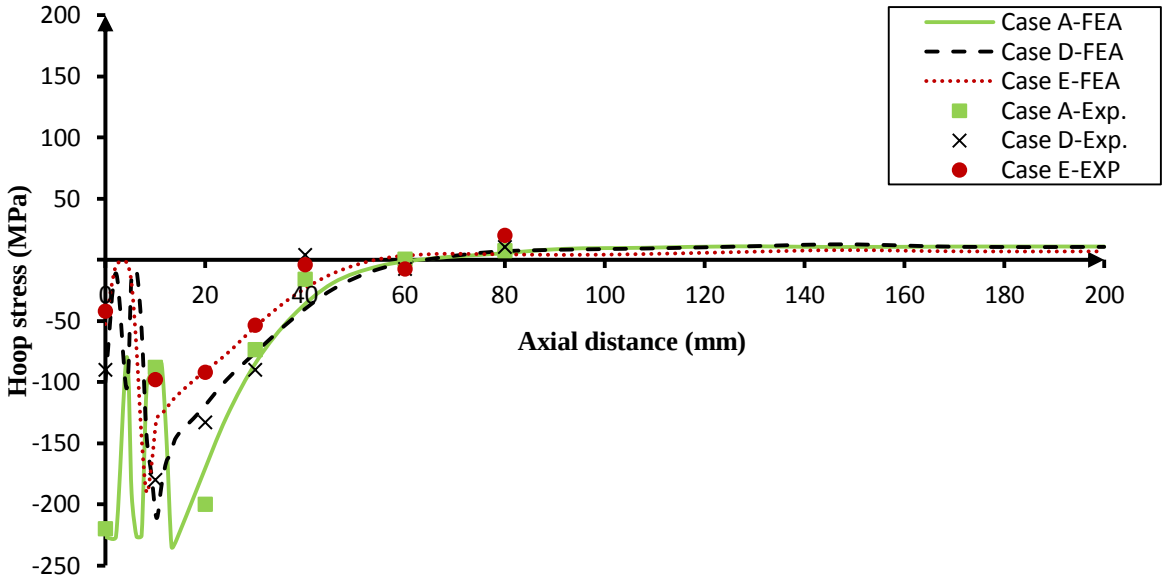

(d)

Fig. 14 Comparison of residual stresses at 270° central angle among case A, case D and case E: (a) axial stress distributions on the inner surface, (b) hoop stress distributions on the inner surface, (c) axial stress distributions on the outer surface, and (d) hoop stress distributions on the outer surface.

4.4.4. Effect of liner on welding residual stress

The function of the liner is to protect the inner surface of the C-Mn pipe from corrosion. With this function, it is made of corrosion resistant alloy CRA, austenitic stainless steel. Consequently, removing the liner will not only lead to corrosion of the pipe in oil and gas applications but it will also affect the residual stress behaviour especially at welding regions [23].

Fig. 15(a)-(d) compares the axial and hoop residual stress distributions on the inner and outer surface numerically and experimentally for case A and case F in which the liner with weld overlay is removed. On the inner surface, the axial residual stress at the WCL in case F, 333 MPa, is lower than that in case A, 540 MPa, as depicted in Fig. 15(a). In the hoop direction, the magnitude of hoop residual stress at the WCL in case F, 364 MPa, is larger than its counterpart in case A, 203 MPa. With increasing distance from the WCL, the hoop residual stress distribution drops rapidly in case F whereas the distribution in case A goes sharply up within the weld overlay region as shown in Fig. 15(b). Furthermore, the extent of the axial and hoop tensile stresses in case F is relatively narrower, Z = 19 mm, than that of case A, Z = 65 mm, on the inner surface as shown in Fig. 15(a) and (b). This can be attributed to the absence of the liner and of the weld overlay at the inner surface which in turn slows down the heat transfer of the exposed surface to the environment.

On the outer surface, the maximum compressive axial stress in case F, -562 MPa, is located within the FZ, at Z = 2.1 mm, whilst the maximum compressive axial stress in case A is located at the WCL, -595 MPa, as shown in Fig. 15(c). In both cases, the hoop residual stress distributions have a wave form as shown in Fig. 15(d). As with tensile stresses at the inner boundary, the compressive range in case F is relatively narrower than that for case A. In general, the numerical residual stress results agree reasonably well with the experimental results obtained by using the hole-drilling strain gauge method.

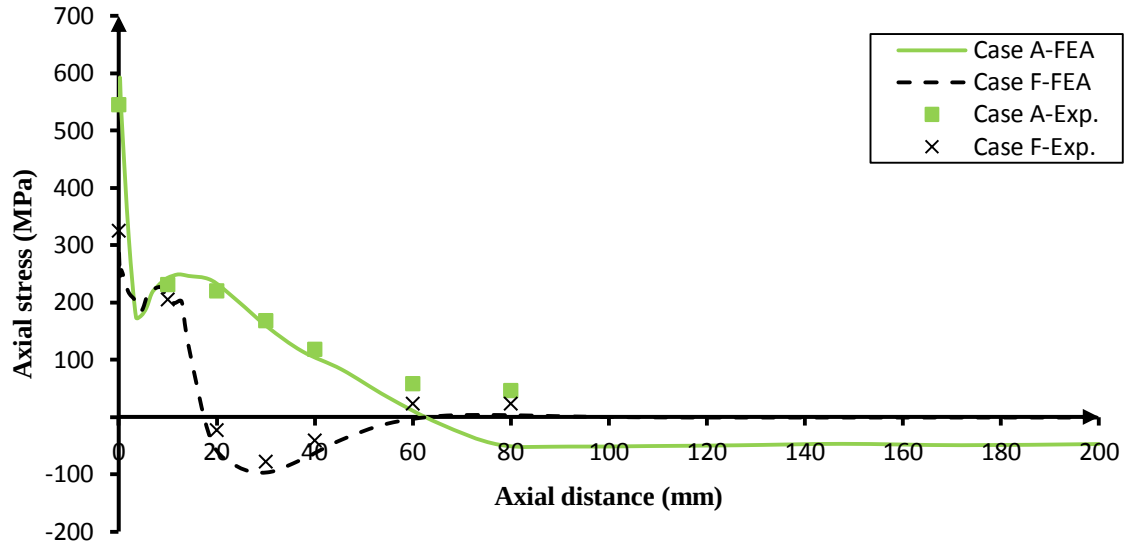

(a)

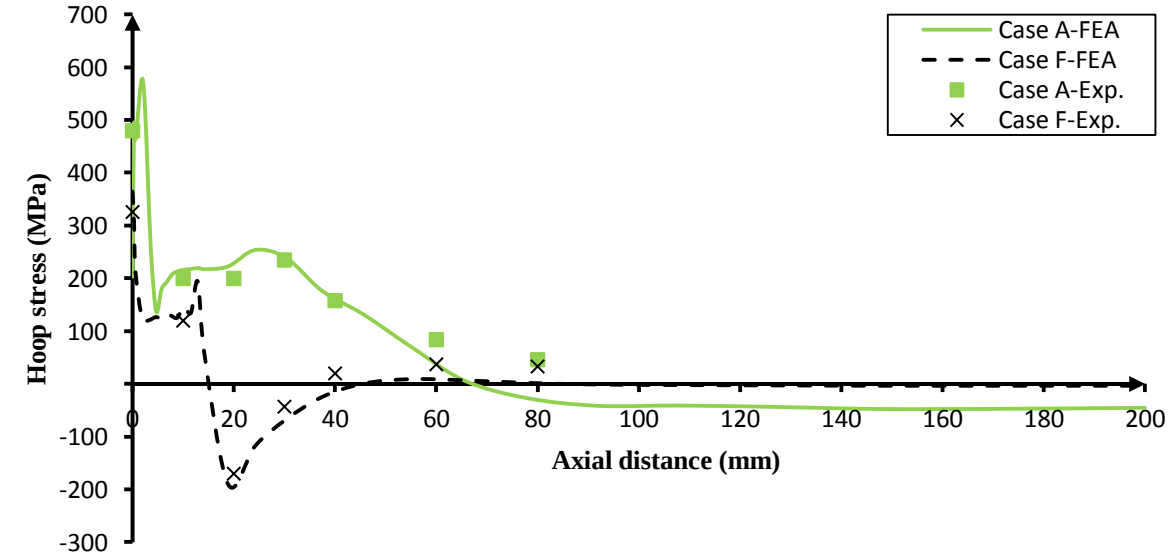

(b)

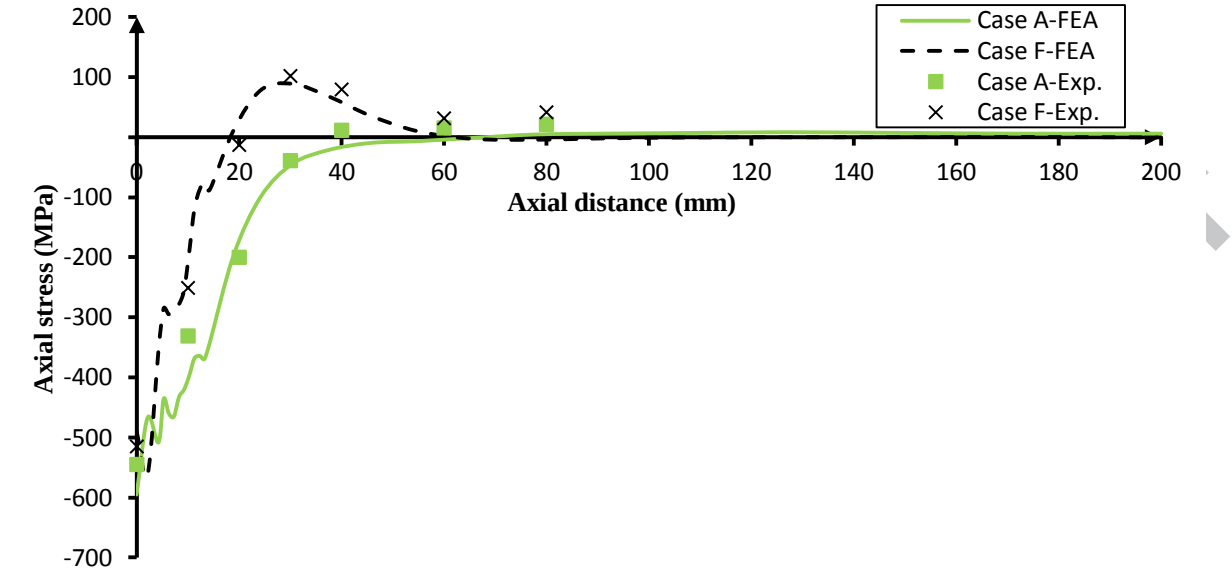

(c)

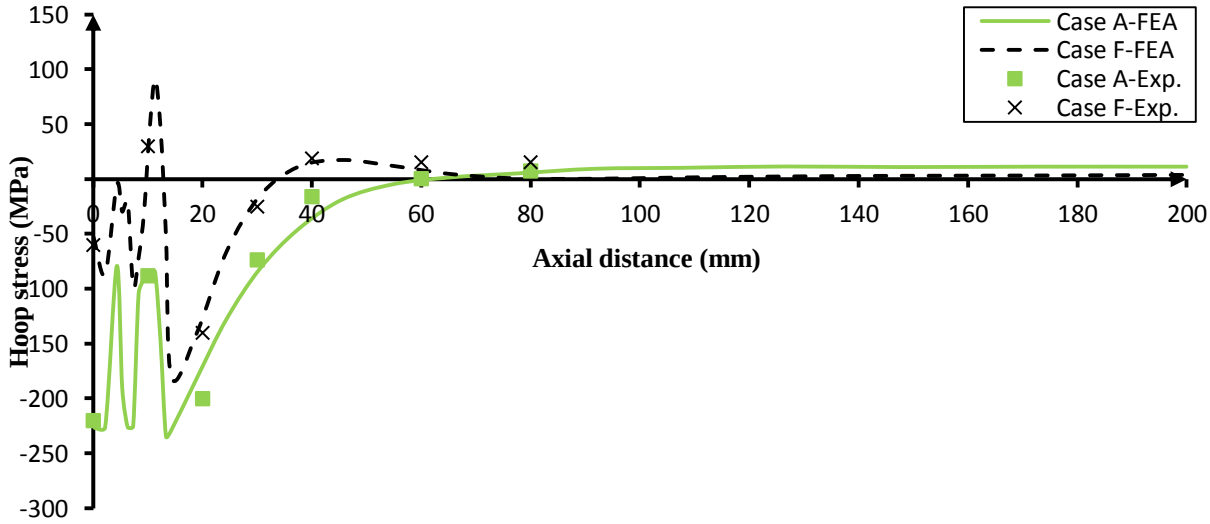

(d)

Fig. 15 Comparison of residual stresses at 270° central angle between case A and case F: (a) axial stress distributions on the inner surface, (b) hoop stress distributions on the inner surface, (c) axial stress distributions on the outer surface, and (d) hoop stress distributions on the outer surface.

5. Mesh convergence analysis

The FE mesh density plays a key role in determining the accuracy of numerical results. To assess such accuracy, a coarse mesh analysis has been used for both the thermal and the mechanical analyses for case A. The coarse mesh model consists of 14000 nodes associated with 2880 elements. The element type is DC3D20 and C3D20 in the thermal and mechanical analyses in ABAQUS, respectively. Also, the element birth technique is adopted in the FEM coarse model to simulate depositing the filler materials in the weld overlay and girth welding while moving the heat source. The coarse mesh size is equal to or larger than 1.5 times the normal mesh size utilized in this study for case A (see Fig. 5) with the coarse mesh model being composed of 40 circumferential elements instead of 60 elements, as shown in Fig. 16.

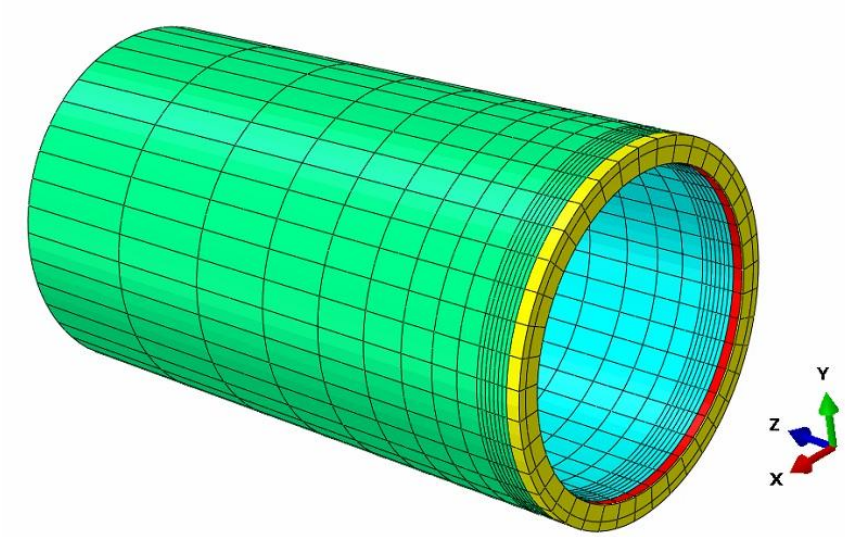

Fig. 16 Coarse 3-D FE model (case A)

In the thermal analysis, Fig. 17 compares the temperature distributions during weld overlay for the coarse mesh model, denoted as 1.5h, against the normal mesh model, denoted as 1h, at 90°, 180° and 270° central angle. The maximum temperature is achieved at the welding pool centre of weld overlay which is 1650°C in the coarse mesh model and 1634°C in the normal mesh model of case A.

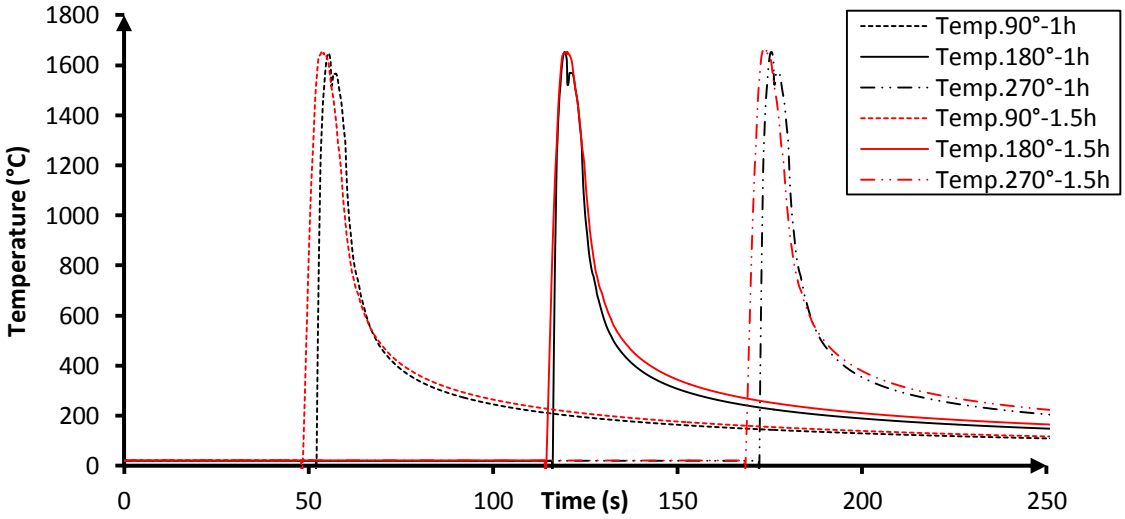

Fig. 17 The thermal history of weld overlay centre at 90°, 180° and 270° central angle for coarse and normal mesh.

Likewise, the temperature fields of the second pass of girth welding also have very similar distributions around lines of symmetry (WCL) at three locations, 90°, 180° and 270° central angle, for the coarse and the normal mesh models. The peak temperature for the coarse mesh is 2085°C whereas the peak temperature for the normal mesh is 2076°C, as shown in Fig. 18.

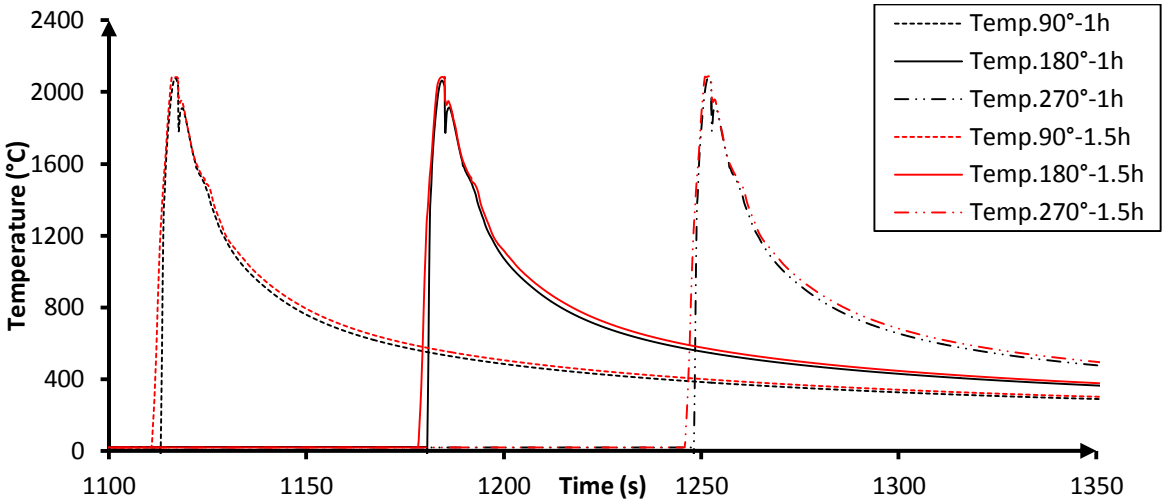

Fig. 18 The thermal history of second pass centre of girth welding at 90°, 180° and 270° central angle for coarse and normal mesh.

One may note that there is a very good correlation in the thermal fields between the coarse mesh and the normal mesh models. As a result, the residual stress distributions on the inner and outer surfaces for the coarse mesh model should also be consistent with the results of the normal mesh model of case A. Fig. 19(a)-(d) plots the residual stress comparisons between the coarse mesh model and the normal mesh model at 270° central angle.

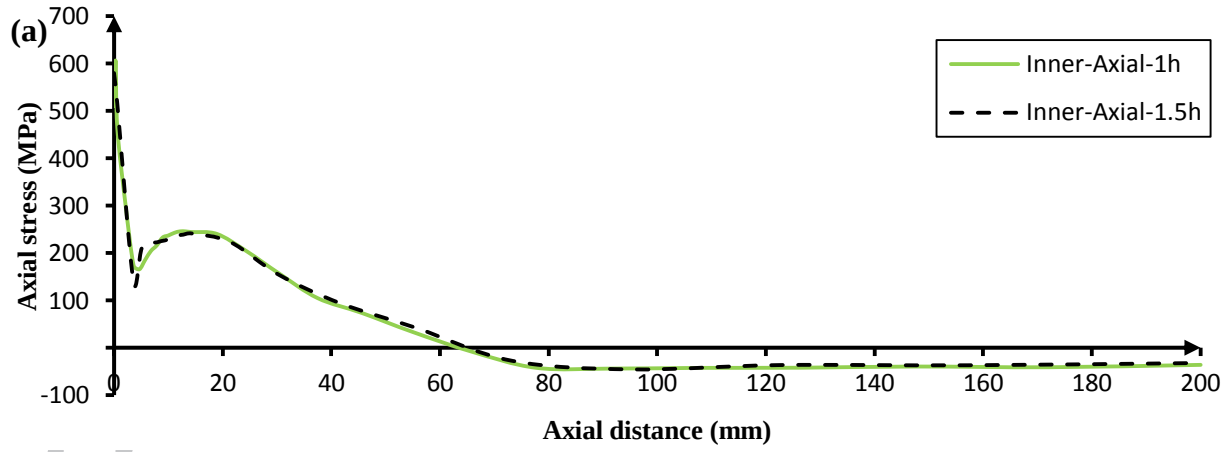

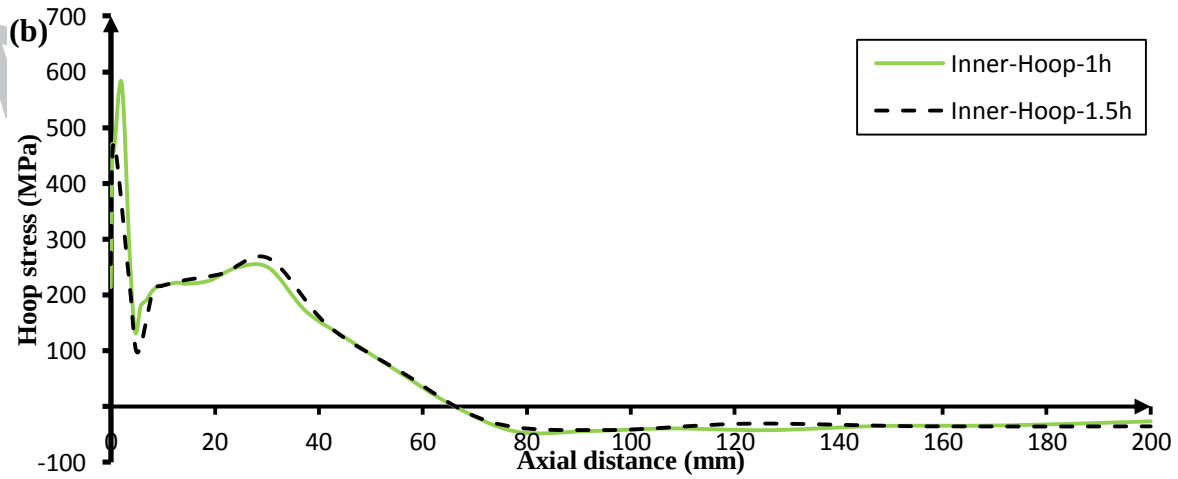

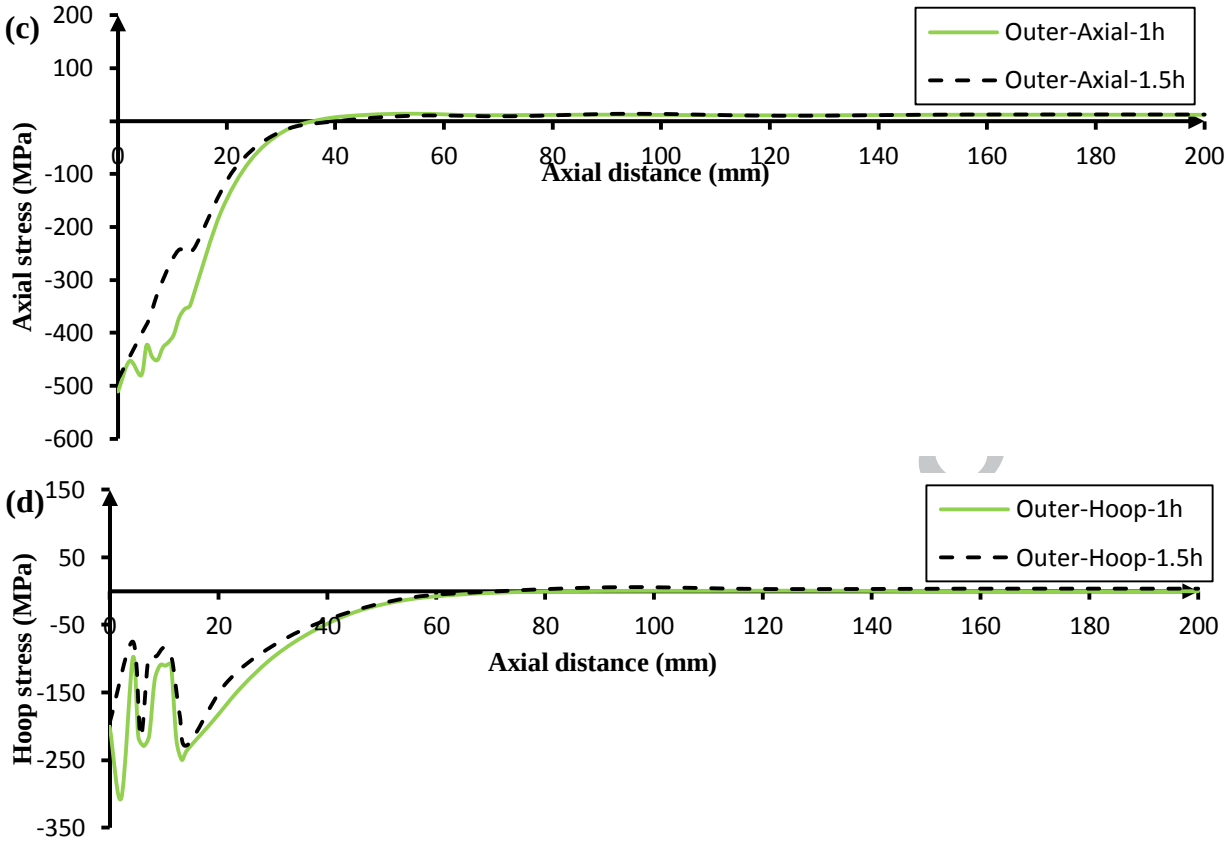

Fig. 19 Residual stress distributions for coarse and normal mesh models at 270° central angle: (a) axial stress distributions on the inner surface, (b) hoop stress distributions on the inner surface, (c) axial stress distributions on the outer surface, and (d) hoop stress distributions on the outer surface.

Consequently, the normal mesh used in cases A, B, C, D, E and F can be considered appropriate to obtain accurate numerical results thermally and mechanically.

6. Radial shrinkage

Moving the heat source circumferentially to deposit the filler materials is mainly responsible for the radial shrinkage during lined pipe welding. In fact, the magnitudes of heat input provided during three welding passes are quite enough for the filler materials to flow through welding regions. Thus, a series of radial expansions is produced due to uniform high temperatures through the pipe thickness. After completing the welding process, subsequent radial contractions take place during solidification and cooling down to room temperature. As a result, a local inward deformation in the weld zones results in a simple linear bending in conjunction with compressive stresses over the outer surface, which are balanced by tensile stresses on the inner surface. Moreover, the magnitude of radial shrinkage is significantly affected by the magnitude of axial stresses. Radial deformations on the inner surface of the lined pipe for six cases at 270° central angle with respect to the longitudinal direction starting from the WCL are plotted in Fig. 20. It is noticeable that the case with a large axial tensile

stress at the WCL has a large radial shrinkage. In other words, larger residual axial tensile stresses on the inner surface lead to larger bending moments at the WCL in conjunction with radial shrinkage.

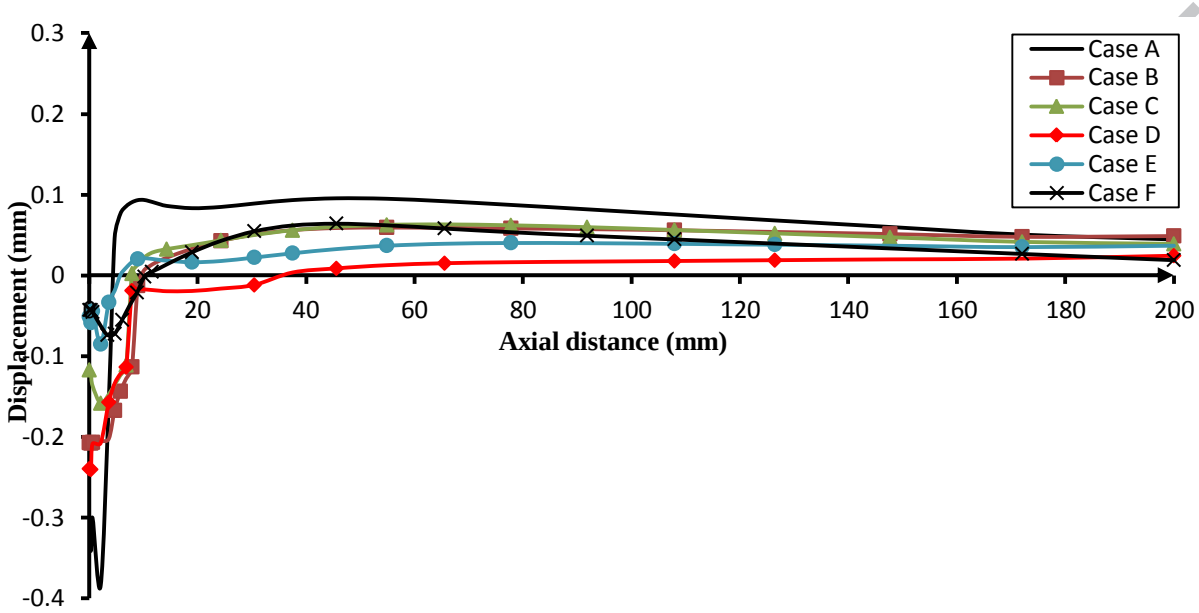

Fig. 20 Radial shrinkage for six cases on the inner surface at 270° from the WCL.

7. Conclusions

In this study, 3-D FE models have been developed and experimental tests have been conducted to study the influence of a number of factors on the thermal and structural response in lined pipe welding. These factors include welding properties (weld overlay and girth welding materials), geometric parameters (using weld overlay and liner) and welding process parameters (heat input). In detail, the thermal history and residual stress distributions have been studied for particular locations on the inner and outer surfaces in comparison with their experimental counterparts, measured using thermocouples and residual stress gauges. Based on the results, the following main conclusions can be drawn:

(1) The numerical thermal results are consistent with the experimental results with a variation of less than 6%. Furthermore, the discrepancies between the thermal results of reference case A and other parametric cases decrease by heading far away from the WCL along the axial direction.

(2) The tensile stresses on the inner surface are balanced by the compressive stresses on the outer surface at the FZ and HAZ to produce local inward deformation through the pipe cross section. The area at which the weld overlay is fixed with the C-Mn pipe is affected by high thermal cycles, which in turn lead to higher hoop and axial tensile residual stresses and possible cracks forming.

(3) Changing the material type for girth welding from carbon steel to stainless steel leads to enhanced corrosion resistance and a reduction in the axial and hoop residual stresses on the inner and outer surfaces at the FZ.

(4) Omitting the weld overlay leads to a significant reduction in the axial and hoop residual stresses at the FZ on the inner and outer surface but the detrimental effect of leaving a gap between liner and C-Mn pipe should be taken into account.

(5) Reducing heat input produces lower residual stresses at the FZ and its vicinity on the inner and outer surface.

(6) The extents of tensile and compressive stresses on the inner and outer surfaces become significantly narrower by removing the liner.

(7) Increasing the residual axial tensile stress leads to an increase in the radial shrinkage at the WCL.

(8) Increasing the element size to 1.5 times the normal one used in this work does not result in a significant change in the results for the thermal conditions and residual stresses.

Acknowledgments

The authors would like to thank all the lab technicians, and in particular Mr Paul Yates, Mr Ali Ahmadnia, Mr Keith Withers and Mr Guy Fitch, for their help and technical advice during the experimental work conducted at Brunel University. The first author also wishes to gratefully acknowledge the financial support provided by Al-Baath University and the British Council.

References

[1] Obeid, O., Alfano, G. and Bahai, H., 2014. Analysis of the temperature evolution during lined pipe welding. In Advanced Materials Research (Vol. 1016, pp. 753-757). *Trans Tech Publications*. doi: 10.4028/www.scientific.net/AMR.1016.753

[2] Karlsson, R.I. and Josefson, B.L., 1990. Three-dimensional finite element analysis of temperatures and stresses in a single-pass butt-welded pipe. *Journal of pressure vessel technology*, *112*(1), pp.76-84. doi: 10.1115/1.2928591

[3] Teng, T.L. and Chang, P.H., 1998. Three-dimensional thermomechanical analysis of circumferentially welded thin-walled pipes. *International Journal of Pressure Vessels and Piping*, *75*(3), pp.237-247. doi: 10.1016/S0308-0161(98)00031-3

[4] Deng, D. and Murakawa, H., 2006. Numerical simulation of temperature field and residual stress in multi-pass welds in stainless steel pipe and comparison with experimental measurements. *Computational materials science*, *37*(3), pp.269-277. doi: 10.1016/j.commatsci.2005.07.007

[5] Yaghi, A.H., Hyde, T.H., Becker, A.A., Sun, W., Hilson, G., Simandjuntak, S., Flewitt, P.E.J., Pavier, M.J. and Smith, D.J., 2010. A comparison between measured and modeled residual stresses in a circumferentially butt-welded P91 steel pipe. *Journal of Pressure Vessel Technology*, *132*(1), p.011206. doi: 10.1115/1.4000347

[6] Dehaghi, E.M., Moshayedi, H., Sattari-Far, I. and Arezoodar, A.F., 2017. Residual stresses due to cladding, buttering and dissimilar welding of the main feed water nozzle in a power plant reactor. *International Journal of Pressure Vessels and Piping*, 152, pp.56-64. doi: 10.1016/j.ijpvp.2017.05.009

[7] Brickstad, B. and Josefson, B.L., 1998. A parametric study of residual stresses in multi-pass butt-welded stainless steel pipes. *International Journal of Pressure Vessels and Piping*, *75*(1), pp.11-25. doi: 10.1016/S0308-0161(97)00117-8

[8] Deng, D., Murakawa, H. and Liang, W., 2008. Numerical and experimental investigations on welding residual stress in multi-pass butt-welded austenitic stainless steel pipe. *Computational Materials Science*, *42*(2), pp.234-244. doi: 10.1016/j.commatsci.2007.07.009

[9] Malik, A.M., Qureshi, E.M., Dar, N.U. and Khan, I., 2008. Analysis of circumferentially arc welded thin-walled cylinders to investigate the residual stress fields. *Thin-Walled Structures*, *46*(12), pp.1391-1401. doi: 10.1016/j.tws.2008.03.011

[10] Lei Zhao, Jun Liang, Qunpeng Zhong, Chao Yang, Biao Sun, Jinfeng Du, 2014. Numerical simulation on the effect of welding parameters on welding residual stresses in T92/S30432 dissimilar welded pipe, *Advances in Engineering Software*, 68, pp.70-79. doi: 10.1016/j.advengsoft.2013.12.004

[11] Velaga, S.K. and Ravisankar, A., 2017. Finite element based parametric study on the characterization of weld process moving heat source parameters in austenitic stainless steel. *International Journal of Pressure Vessels and Piping*. doi: 10.1016/j.ijpvp.2017.09.001

[12] Obeid, O., Alfano, G. and Bahai, H., 2017. Thermo-Mechanical Analysis of a Single-Pass Weld Overlay and Girth Welding in Lined Pipe. *Journal of Materials Engineering and Performance*, 26(8), pp.3861-3876. doi: 10.1007/s11665-017-2821-5

[13] Ma, N., Li, L., Huang, H., Chang, S. and Murakawa, H., 2015. Residual stresses in laser-arc hybrid welded butt-joint with different energy ratios. Journal of Materials Processing Technology, 220, pp.36-45. doi: 10.1016/j.jmatprotec.2014.09.024

[14] Focke, E.S., 2007. Reeling of tight fit pipe. TU Delft, Delft University of Technology.

[15] ABAQUS Documentation, release 14. Dassault Systèmes, Providence, RI.

[16] Deng, D., 2009. FEM prediction of welding residual stress and distortion in carbon steel considering phase transformation effects. Materials & Design, 30(2), pp.359-366. doi: 10.1016/j.matdes.2008.04.052

[17] Yaghi, A.H., Tanner, D.W.J., Hyde, T.H., Becker, A.A. and Sun, W., 2011, May. Abaqus Thermal Analysis of the Fusion Welding of a P92 Steel Pipe. In SIMULIA Customer Conference (pp. 622-638).

[18] Hempel, N., Bunn, J.R., Nitschke-Pagel, T., Payzant, E.A. and Dilger, K., 2017. Study on the residual stress relaxation in girth-welded steel pipes under bending load using diffraction methods. *Materials Science and Engineering: A*, 688, pp.289-300. doi: 10.1016/j.msea.2017.02.005

[19] Nasim, K., Arif, A.F.M., Al-Nassar, Y.N. and Anis, M., 2015. Investigation of residual stress development in spiral welded pipe. *Journal of Materials Processing Technology*, 215, pp.225-238. doi: 10.1016/j.jmatprotec.2014.08.009

[20] Xu, J., Chen, J., Duan, Y., Yu, C., Chen, J. and Lu, H., 2017. Comparison of residual stress induced by TIG and LBW in girth weld of AISI 304 stainless steel pipes. *Journal of Materials Processing Technology*. doi: 10.1016/j.jmatprotec.2017.05.014

[21] Benson, D., 2014. Tips for Successfully Welding Stainless Steel to Carbon Steel. *Welding journal*, 93(5), pp.54-56.

[22] Hemmatzadeh, M., Moshayedi, H. and Sattari-Far, I., 2017. Influence of heat input and radius to pipe thickness ratio on the residual stresses in circumferential arc welded pipes of API X46 steels. *International Journal of Pressure Vessels and Piping*, 150, pp.62-71. doi: 10.1016/j.ijpvp.2017.01.001

[23] Hilberink, A. (2011). Mechanical behaviour of lined pipe (Doctoral dissertation, TU Delft, Delft University of Technology).

Highlights

- Six parametric cases have been discussed and compared thermally and mechanically.
- The numerical thermal results are consistent with the experimental results.
- The meeting area between the weld overlay and the C-Mn pipe is likely being cracked.